INVESTIGATING ELECTRONIC PEDESTALS OF THE ANALOGUE FRONT-END BOARDS OF THE UPGRADED HIGH-ENERGY STEREOSCOPIC SYSTEM (H.E.S.S-I) CAMERAS

A THESIS SUBMITTED IN PARTIAL FULFILMENT

OF THE REQUIREMENTS FOR THE DEGREE OF

MASTER OF SCIENCE IN PHYSICS

OF

THE UNIVERSITY OF NAMIBIA

BY

KLEOPAS PANDENI SHININGAYAMWE

200970763

APRIL 2017

Supervisor: Dr M. Backes

UNAM, Department of Physics, Windhoek, Namibia

Abstract

The High-Energy Stereoscopic System (H.E.S.S.) is an array of five imaging atmospheric Cherenkov telescopes located in the Khomas Highland in Namibia, dedicated to very-high-energy (VHE, 100 GeV – 100 TeV) gamma-ray astronomy. It consists of four identical 12 m diameter telescopes (H.E.S.S.-I) which started operating in 2003 and a large 28 m diameter telescope (H.E.S.S.-II) which was brought online in 2012 [1].

The H.E.S.S.-I camera upgrade project was aimed to increase the stability and performances of the camera operation by replacing the 13 years old camera electronics with modern-day technologies. The most delicate part of the upgraded electronics are the readout boards of the drawers, which have been upgraded with a new analog memory [2, 3]. A significant level of cross-talk has been observed in the analog front-end boards of the H.E.S.S.-I camera upgrade [3], and investigating the electronic pedestals of these analog boards could help understand the origin of such a cross-talk. A C++ code written in ROOT modular scientific software framework has been developed for the analysis of the data taken with a drawer on the Test bench at DESY in Zeuthen, Germany. So far, from the computation of the autocorrelation function and Fourier transform of the electronic pedestals, no characteristic patterns have

been found to explain the level of cross-talk observed. The upgrade of the cameras is ongoing, and the investigations of the noise level of the rear part of the electronic boards will be continued.

Contents

Acknowledgements

I would like to express my greatest gratitude to the people who have helped and supported me throughout my project. Many thanks to my supervisor, Dr. Michael Backes, who read many drafts of my project and helped me make some sense out of the confusion. Thanks to the H.E.S.S. group at DESY in Zeuthen, Germany, for accepting me and making me feel one of them during the Summer studentship I had at DESY. My special thanks go to Dr. Stefan Klepser as well as to Dr. Stefan Ohm of DESY, who gave me the golden opportunity to do this wonderful project, which also helped me in doing a lot of research and I came to know about so many new things, I am really thankful to them. I would also like to express my deepest gratitude and special thanks to Dr. Simon Bonnefoy of DESY, who despite being extraordinarily busy with his duties, took time out to hear, guide and keep me on the correct path and allowing me to carry out my project. Without his passionate participation and input, this project could not have been successfully conducted. I will strive to use gained skills and knowledge in the best possible way in order to attain desired career objectives. I hope to continue cooperation with all of you in the future.

I would like to thank UNAM for allowing me to attend the Summer Student programme at DESY, DESY and the NCRST for providing me with the financial means to complete this project.

Declarations

- I, Kleopas Pandeni Shiningayamwe, declare hereby that this study is a true reflection of my own research, and that this work, or part thereof has not been submitted for a degree in any other institution of higher education.
- No part of this thesis may be reproduced, stored in any retrieval system, or transmitted in any form, or by means (e.g. electronic, mechanical, photocopying, recording or otherwise) without the prior permission of the author, or The University of Namibia in that behalf.
- I, Kleopas P. Shiningayamwe, grant The University of Namibia the right to reproduce this thesis in whole or in part, in any manner or format, which The University of Namibia may deem fit, for any person or institution requiring it for study and research; providing that The University of Namibia shall waive this right if the whole thesis has been or is being published in a manner satisfactory to the University.

Signature:... Date:..................................

Mr. Kleopas Pandeni Shiningayamwe

List of acronyms

ADC Analog to Digital Converter,

ANTARES Astronomy with a Neutrino Telescope and Abyss environmental RESearch project,

ARS0 Analog Ring Digital Sampling memory, a 4 channels analogue memory used as a circular buffer, which was originally developed for the ANTARES experiment by the CEA/DAPNIA–SEI,

CT Cherenkov Telescope,

CTA Cherenkov Telescope Array,

DAQ Data Acquisition,

DESY Deutsches Electronen-Synchrotron, in English: German Electron Synchrotron, a national research center in Germany that operates particle accelerators used to investigate the structure of matter.,

EGRET Energetic Gamma Ray Experiment Telescope,

FPGA Field Programmable Gate Array, an electronic component within which logical functions can be programmed,

***Fermi*-LAT** The Large Area Telescope is the principal scientific instrument on the Fermi Gamma Ray Space Telescope spacecraft which is used to perform gamma-ray astronomy observations near the Earth orbit.,

H.E.S.S. High Energy Stereoscopic System,

HESS-I H.E.S.S. Phase one,

HESS-II H.E.S.S. Phase two,

IACT Imaging Atmospheric Cherenkov Telescope,

MAGIC Major Atmospheric Gamma Imaging Cherenkov,

NCRST National Commission on Research Science and Technology,

NECTAr New Electronics for the Cherenkov Telescope Array,

PMT Photo Multiplier Tube,

UNAM The University of Namibia,

VERITAS Very Energetic Radiation Imaging Telescope Array System.

Prefixes: 10^{-9} nano n, 10^{-6} micro μ, 10^{3} kilo k, 10^{6} mega M, 10^{9} giga G

Conversion factors: 1 GeV = 10^{9} eV, 1 TeV = 10^{12} eV, 1 eV = 1.602×10^{-19} J

Constants: $c = 2.998\times10^{8}$ m/s, $e = 1.602\times10^{-19}$ C, $h = 6.626\times 10^{-34}$ J·s, $\hbar = 2\pi h$

List of Figures

Chapter 1

Introduction

This thesis begins with a brief astrophysical motivation for the investigation of cosmic particle accelerators using very high-energy gamma rays. The production mechanisms of very high-energy gamma rays and their detection on Earth using Cherenkov telescopes will be discussed. The H.E.S.S. experiment, which is a system of 5 Imaging Atmospheric Cherenkov Telescopes (IACTs) will be discussed.

The H.E.S.S. experiment in the Khomas Highland in Namibia is investigating cosmic particle accelerators by scanning the southern sky in the very high-energy gamma-ray band. Many of the objects that were detected using the H.E.S.S. telescopes are pulsar wind nebulae within our own Galaxy, the Milky Way, and some of them are within only few hundred light-years from Earth [1]. As MAGIC [4] and VERITAS [5] in the past years, also the H.E.S.S. telescopes, in particular, H.E.S.S.-I, underwent a substantial hardware upgrade in July 2015 and September 2016 to optimise its performance in its final years.

The H.E.S.S.-I camera upgrade was aimed to reduce the dead time of its individual cameras, in order to make it comparable to that of CT5. Another aim was to reduce the downtime of the cameras, induced by their ageing and increasing failure rates of cable connectors and other critical parts [2]. In order to achieve these aims of the upgrade, the initial readout scheme which was based on the ARS0 chip [6] was replaced with a fast, ethernet-based readout and modern front-end boards built around the NECTAr (New Electronics for the Cherenkov Telescope Array) analog readout chips [2].

A significant level of cross-talk has been discovered in the new analog boards of the upgraded cameras. This study is focused on understanding the origin of the cross-talk observed in the front-end readout electronics board of the H.E.S.S.-I camera upgrade. In order to understand the origin of such a cross-talk, electronic pedestals of the analog front-end readout boards of the camera are studied. The statistical study of these electronic pedestals is discussed in chapter 5 . At last, the results of the statistical study of the electronic pedestals of the analog front-end readout boards will be presented in chapter 6.

Chapter 2

Literature Review

2.1 Astrophysical motivation

The study of very-high-energy physics is motivated by the desire to understand where and how particle acceleration is taking place in extreme astrophysical environments [7]. Typical examples of extreme environments where particles may be accelerated include supernova remnants, rotation-powered pulsar wind-nebulae, stellar associations and sources with relativistic jet outfows such as microquasars and the central regions of active galaxies. The sources as well as the physical mechanism(s) responsible for endowing cosmic ray particles with enormous energies are yet not well understood [8].

Charged cosmic rays are continuously deviated by turbulent magnetic fields embedded in interstellar and intergalactic plasmas, so their direction when they reach the Earth is almost completely uncorrelated (they are isotropically distributed) with that of their source, except perhaps at extreme energies where the fluxes are extremely low [9]. For locating the source of high-energy particles measured on Earth, it is necessary to follow up the track of the corresponding particle. Often, a source of charged high-energy particles is also a source of high-energy photons (see section 2.3 for their production mechanisms). Since the universe is almost transparent gamma rays, the quest for cosmic accelerators as well as for acceleration mechanisms of cosmic rays mostly relies on high-energy photons (and neutrinos) which propagate along straight lines and thus do not lose their direction information even when putting back a huge distance.

2.2 The cosmic ray spectrum

Studying the energy spectrum (and chemical composition) of cosmic rays may give a better understanding on how they are accelerated and how they propagate from their original sources. In the last decades, experiments such as AUGER and HiRes have measured particles with much higher energies up to 10^{20} eV (see Fig. 2.1) [10, 11]. The energy distribution of cosmic rays is well described by a power law. The origin of the observed changes in the steepness of the spectrum is still the subject of intense study, but it is assumed that they distinguish between populations of cosmic rays originating via different mechanisms [11, 12].

Current suggestions are that the cosmic rays with energies less than $\sim 10^{10}$ eV are primarily solar cosmic rays produced in solar ares and coronal mass ejections [13], while those with energies between 10^{10} eV and the knee, at 10^{15} eV, are galactic cosmic rays produced in the shocks of supernova remnants. The origin of the cosmic rays with energies between the knee and ankle remains unclear. They are again thought to be produced within the Galaxy, but the energies are too high for them to be accelerated by the shocks of supernova remnants. The origin of the ultra-high-energy cosmic rays (UHECRs) above the *ankle* is also a mystery, but many have suggested that these may be created outside of our Galaxy [10].

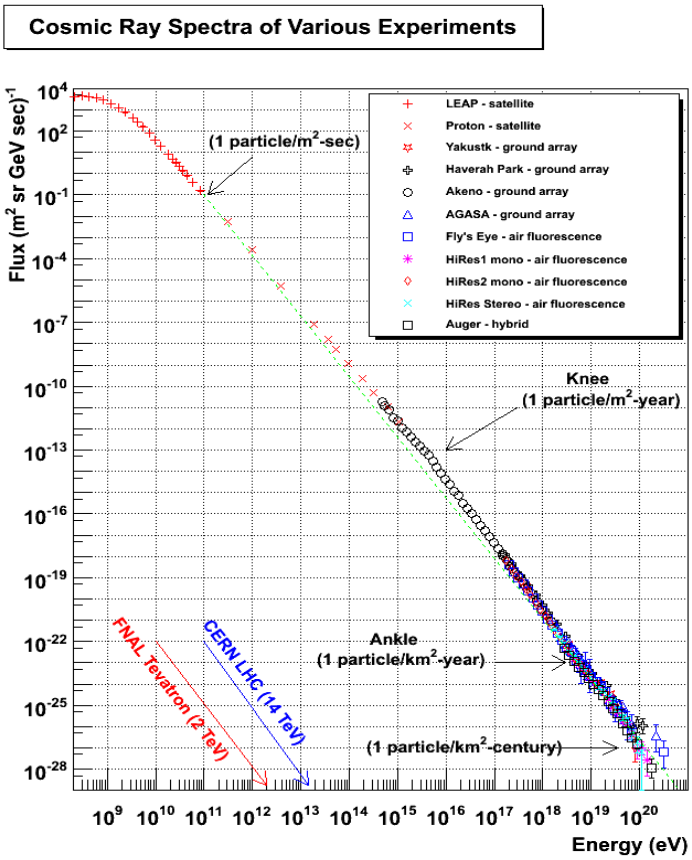

Figure 2.1. The energy spectrum of cosmic rays. Data from different experiments are shown by different symbols. The spectrum clearly shows that the number of cosmic rays drops off dramatically at higher energies. The *knee* and *ankle* are clearly visible on the spectrum [10].

The existence of UHECRs with energies above 5×10^{19} eV remains a mystery. At energies beyond this Greisen-Zatsepin-Kuzmin limit (GZK limit), the cosmic ray should interact with the radiation of the cosmic microwave background (2.7 K) within a distance of 150 million light-years and lose energy. This would reduce the energy of the cosmic ray to below the GZK limit, and particles with energies up to 10^{20} eV should not have been observed if they come from distant sources [11].

2.3 Gamma-rays production mechanisms

High-energy gamma rays have been detected from emissions of astronomical sources such as supernova explosions, neutron stars, and quasars. However, these gamma rays are not produced directly by the sources of the cosmic radiation, they can be created as secondaries of high-energy cosmic rays. Gamma rays can be produced for instance during particle-particle collisions, where a high-energy proton, or cosmic ray, strikes another proton or atomic nucleus. This collision produces secondary particles, which may include one or more neutral π-mesons (or pions) [14–16]. The resulting pions can further decay into a pair of gamma rays ($\pi^0 \rightarrow 2\gamma$). Also, if a primary accelerator generates a beam of high-energy electrons, these electrons may undergo bremsstrahlung in the ambient medium, may suffer synchrotron radiation losses in local magnetic fields, or may, via the inverse Compton scattering process, transfer a significant part of their energy to an ambient photon, which then emerges as a high energy gamma ray [17].

2.4 The imaging atmospheric Cherenkov technique

The Earth atmosphere is opaque to photons beyond the optical waveband, thus high-energy astrophysics require the advent of space-based experiments. Since the flux of gamma rays decreases rapidly with increasing energy (as seen in Fig. 2.1), space-based instruments such as EGRET [18] and *Fermi*-LAT [19] can only efficiently explore the energy band from about 0.5 MeV up to below

$\sim$ 100 GeV, called the high-energy (HE) gamma-ray domain as opposed to the very-high-energy domain (VHE, 100 GeV – 100 TeV), for which ground-based detectors are required.

The key advantage of ground-based experiments over satellite-based experiments is the collection area. The problem with satellite experiments is that they only have an effective area in the order of square meters. If the flux of gamma rays at very-high energies is small, one needs a big effective area to get an acceptable rate. Therefore one uses Imaging Atmospheric Cherenkov Telescopes (IACT) which provide an effective area in the order of $> 10^5$ m^2. Currently, the three major Cherenkov telescope systems in use are VERITAS, MAGIC, and H.E.S.S., all of them having multiple telescopes to allow the use of stereoscopy.

2.4.1 Electromagnetic shower formation

When a very-high-energy gamma ray (primary) interacts with the atmospheric nuclei (this can happen at an altitude of about 10 – 20 km above sea level), it initially generates an electron and positron pair, via pair production. Each high-energy $e^{\mp}$ radiates secondary gamma rays through bremsstrahlung, which further convert into $e^+ + e^-$ pairs of lower energies (see Fig. 2.2). This process continues until the average energy per particle drops below 80 MeV [20]. At this point, the interactions lead to the absorption of particles and the cascade begins to die. This altitude is known as the shower maximum, occurring typically at an altitude of $\sim$10 km above sea level [14].

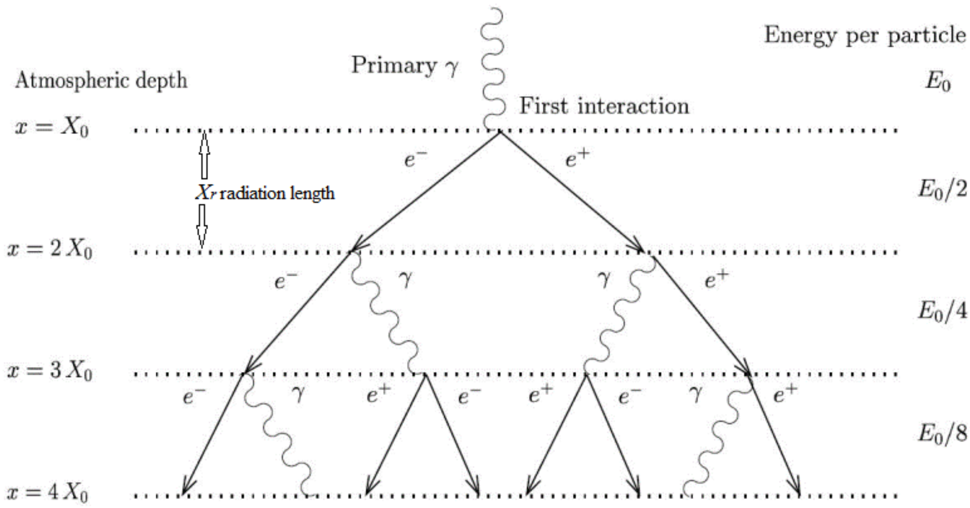

Figure 2.2. Schematic view of an electromagnetic cascade [20]. It should be noted that this is just an illustrative model but not the state-of-art of current air shower knowledge.

Fig. 2.2 is the simple model that illustrates the characteristic longitudinal shower development of a photon induced airshower. The model assumes a cascade, starting with the pair production of an electron and positron, which radiate bremsstrahlung in the second step, and so forth. E0 is the energy of the primary gamma ray. X_0 is the distance over which an electron or positron loses, on average $\langle E \rangle$,

$$\langle E \rangle = E_0 e^{-\frac{X}{X_r}}, \tag{2.1}$$

half of its energy by radiation. After traveling the same distance, X_0 , a photon splits into an $e^+ + e^-$ via pair production. In either instance, the energy E_0 of a particle (electron or photon) is assumed to be equally divided between two outgoing particles, which lead to an energy

$$E_n = 2^{-n} E_0, \tag{2.2}$$

of the particles in a shower after n radiation lengths. The number of particles N in the shower after n radiation lengths is

$$N = 2^n. \tag{2.3}$$

Multiplication of particles ceases when their energies are too low for pair production or bremsstrahlung, at around $E < 80$ MeV [20, 21].

2.4.2 Cherenkov Radiation

In a dielectric medium, the speed of light c is lower than in a vacuum. The charged particles (electrons and positrons) traversing a medium with refractive index $n > 1$ at a speed v, higher than the speed of light in the medium $\frac{c}{n}$, causes the emission of a characteristic electromagnetic radiation, the so-called Cherenkov radiation [22, 23].

Before starting the description of the Cherenkov effect, it must be noted that the Cherenkov radiation is entirely unrelated to the bremsstrahlung, which is emitted by the moving electron itself when it collides with atoms in the medium. The Cherenkov effect involves radiation emitted by the medium under the action of the field of the particle moving in it [9].

If a charged relativistic particle travels through a medium, which can be polarized, it moves other charged particles in the medium out of their rest positions, inducing dipoles along its path. Upon relaxation of those dipoles, spherical waves are emitted. However, if the speed of the charged relativistic particle becomes bigger than the speed of light in the medium, the elementary waves interfere constructively and Cherenkov radiation is emitted [23–25].

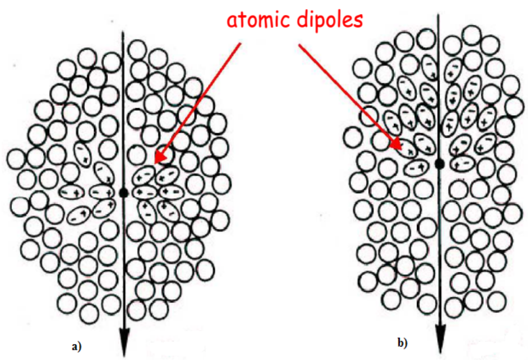

Figure 2.3. Polarization of a medium of refractive n by an electron traveling at speed v [26].

In Fig. 2.3, a), the electron has a speed less than the speed of light in air, i.e $v < \frac{c}{n}$. As a result, the dipole distribution is symmetric around the position of the particle (back and front) and the sum of all dipoles vanishes, and no Cherenkov radiation occurs. However, if $v > \frac{c}{n}$ (as in Fig. 2.3 b) the distribution is asymmetric and the total time-dependent dipole does not vanish and thus radiation of Cherenkov photons occur [26].

Cherenkov light is emitted into a forward cone of aperture $\cos(\theta_c) = \frac{1}{n \cdot \beta}$, where $\beta = \frac{v}{c}$. The condition for Cherenkov radiation emission is that $\beta \geq \frac{1}{n}$. The Cherenkov angle θ_c depends on the refractive index n and grows with increasing particle speed v. If the particle is ultra-relativistic, $\beta \approx 1$, θ_c = constant and has maximum value.

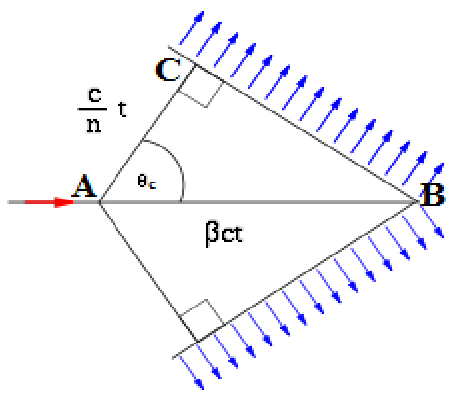

Figure 2.4. Illustration of the formation of the Cherenkov wave front [24].

The wavefront (analogous to shock wave for supersonic aircraft) is emitted at a well defined angle θ_c with respect to the trajectory of the particle. In Fig. 2.4, a particle (arrow) traveling from point A to B in time t has velocity βc. The distances AB and AC are given by $AB = \beta ct$ and $AC = \frac{c}{n}t$. Since $\cos\theta = \frac{AB}{AC}$, making the right substitution gives $\cos\theta = \frac{1}{\beta n}$, which is the criterion for Cherenkov light emission.

If the medium is transparent the Cherenkov light can be detected. This light can be collected by special telescopes even if the electrons and positrons of the shower do not reach the ground. The effective detection area is comparable to that of the light pool on the ground, i.e. about 10^4 m^2, adapted to the very-low gamma-ray fluxes above 100 GeV [24].

The intensity of the Cherenkov radiation (number of Cherenkov photons emitted per unit path length and per wavelength interval) by a particle with charge Z can be calculated with the Frank-Tamm formula: (α is the fine structure constant, $\alpha = \frac{e^2}{\hbar \cdot c} = \frac{1}{137}$) [27]

$$\begin{aligned} \frac{d^2N}{dxd\lambda} &= \frac{4\pi^2 Z^2 e^2}{hc\lambda^2}(1 - \frac{1}{\beta^2 n^2(\lambda)}) \\ &= \frac{2\pi Z^2}{\lambda^2}\alpha(1 - \cos^2(\theta_c)) \\ &= \frac{2\pi Z^2}{\lambda^2}\alpha \sin^2(\theta_c) \end{aligned} \tag{2.4}$$

Equation 2.4 shows that the number of photons per unit length and radiation wavelength depends on charge and velocity of particle. Cherenkov light is proportional to a λ^{-2} power law, where λ is the wavelength. Due to the factor $\frac{1}{\lambda^2}$, the maximum of the distribution $\frac{d^2N}{dxd\lambda}$ is reached for short wavelengths. That is, the greater part of Cherenkov photons are emitted in the blue and ultraviolet range, and the spectrum has a peak at around 330 nm [24].

2.4.3 Detection of high-energy gamma rays using Imaging Atmospheric Cherenkov Telescopes

High-energy gamma rays are too difficult reflect or focus like other forms of light (e.g. optical light and soft x-rays), instead, they are imaged indirectly.

A high energy photon produces a cone of Cherenkov light confined to 1° of the original photon direction [28]. Cherenkov radiation (∼100 photons/m^2/TeV) created in the electromagnetic air showers almost uniformly illuminates a circle of radius $r \approx 120$ m on the ground in a time typically of the order of 10 ns [16,29].

A telescope (like the H.E.S.S. telescopes) located at some altitude above the sea level will detect this Cherenkov light pool and reflect it to its camera, located at the focal point of its reflecting surface (mirror).

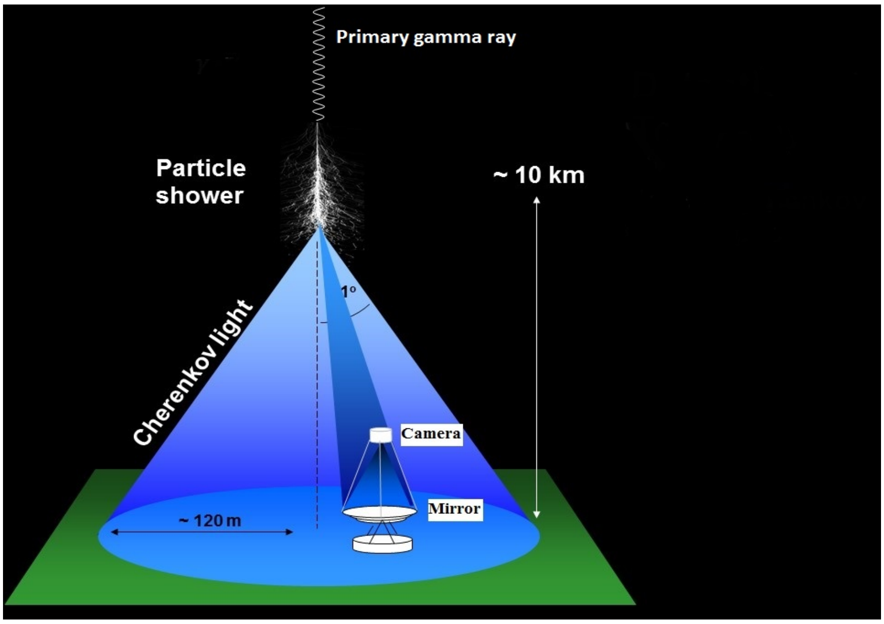

Figure 2.5. Production of Cherenkov light and its detection by the Cherenkov telescopes [28].

In Fig. 2.5, Cherenkov light gets imaged by a large mirror onto a fast camera located at the focal plane of the reflecting mirror. Electromagnetic air showers generate elongated, roughly elliptical images. The major axis of the ellipse represents the shower axis, pointing towards the image of the source on one side. The ellipse is parameterized according to Hillas [30, 31], and this parametrization is used for reconstruction of the shower direction and separation of electromagnetic from hadronic showers.

The use of several telescopes observing the same shower in coincidence allows a unique determination of the shower direction (see Fig. 2.6) by projecting the images in all triggered telescope cameras into one camera. Then the intersection point of the image major axes yields the shower direction. The energy of the primary gamma ray can be determined from the intensity of the Cherenkov light detected [30].

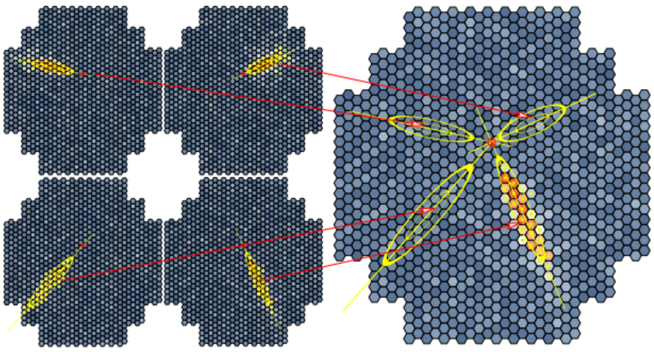

Figure 2.6. Projection of 4 telescope images from within the light pool of an event into one camera plane in a stereo system. Different colors on the PMTs indicate the intensity of photo electrons detected [16].

Unfortunately, not all air showers seen are initiated by gamma rays. In fact, only a tiny fraction of them are. This is because the showers can also be formed when cosmic ray particles (mainly protons) interact with the atmosphere, but these showers can be distinguished based on the shape of the image of the light flash [32]. When compared to proton and nuclei induced air showers, photon induced air showers contain only electrons, positrons and photons (see Fig. 2.2) [14, 22]. Also, gamma ray induced air showers are more compact, more uniform and decay faster. Having more than one telescope simultaneously observing the same spot can also help exclude cosmic rays.

Chapter 3

The High-Energy Stereoscopic System

The High-Energy Stereoscopic System (H.E.S.S.) is an array of 5 Imaging Atmospheric Cherenkov Telescopes (IACTs) (shown in Fig. 3.1), located in the Khomas Highland in Namibia, dedicated to Very-high-energy gamma-ray astronomy. H.E.S.S. is the only IACT system featuring telescopes of different sizes, which provides sensitivity for gamma rays across a very wide energy range, from $\sim$30 GeV up to $\sim$100 TeV [2]. The H.E.S.S. array consists of four identical 12 m diameter telescopes (H.E.S.S.-I or CT1–4) which started operating in 2003 [33] and a large 28 m diameter telescope (H.E.S.S.-II or CT5) which was brought online in 2012 [34]. H.E.S.S.-II was built to reach an energy threshold of $\sim$30 GeV, connecting the energy range of H.E.S.S. to that of satellite experiments like *Fermi*-LAT [34] and giving access to new objects such as pulsars and Active Galactic Nuclei at larger red shifts [35]. So far H.E.S.S. has been the most successful experiment in the field of very-high-energy gamma-ray astronomy, having discovered more than 80 gamma-ray sources.

H.E.S.S. is the 3[rd] generation ground-based atmospheric Cherenkov detector, operated by an international collaboration of over 250 scientists, from 40 scientific institutions and 13 different countries [1, 36]. The basic physics goal of the H.E.S.S. experiment is to explore the production and propagation of very high energy particles in the Universe, i.e. to explore the Non-thermal Universe [1].

Figure 3.1. The H.E.S.S. telescope system in the Khomas highland of Namibia, located at an elevation of 1.8 km above sea level. H.E.S.S.-I is arranged in a square of 120 m sides operating in stereoscopic mode, with CT5 at the center of the array [1]. This setup was chosen because the typical radius of the cone of Cherenkov light is ≈120 m. Also, this setup allows for multiple telescopes to observe the same Cherenkov event, allowing the use of stereoscopy.

Each telescope of H.E.S.S.-I is equipped with a mirror area of 107 m^2, and has a focal plane at 15 m distance from the mirrors where a camera is installed. The reflectors comprise 380 quartz-coated round facets (60 cm diameter each), arranged with Davies-Cotton optics [37].

3.1 H.E.S.S.-I camera upgrade

Since the camera electronics of H.E.S.S.-I are 10 years older than that of CT5, an upgrade of the camera electronics of H.E.S.S.-I was carried out in 2015 and 2016 [2, 3]. In contrast to H.E.S.S.-I, CT5 was not only equipped with more modern camera electronics, but also operates at a much lower energy threshold of ∼30 GeV [38], and therefore delivers much higher rate of air shower triggers as the flux of air showers follow a power law ($\frac{dN}{dE} \propto E^{\gamma}$) in energy with a spectral index γ ≈ -2.5 [39, 40].

The H.E.S.S.-I camera upgrade project aimed to increase the stability and performance of the camera operation by replacing the 13 years old electronics with modern-day technologies [2]. The upgrade is expected to extend the lifetime and reliability of the 13-year old H.E.S.S.-I telescope array until and possibly beyond the expected completion of the upcoming Cherenkov Telescope Array (CTA) observatory in 2018, thereby assuring continuous of very-high energy gamma ray observations of the southern sky with a sensitivity of 1% of the flux of the Crab Nebula in 50 hrs of observation time to be detected with 5 σ significance during the delicate transition phase from the third to the fourth generation of the IACTs [2, 41].

The second goal of the upgrade was to reduce the dead time of the H.E.S.S.-I readout (which was 450 μs) to match that of CT5 which is 15 μs [2, 34]. This is necessary because the central trigger rate of the *full array* has been dominated by the H.E.S.S.-II rate, which could go above 1.5 kHz [3], depending on the trigger threshold setting. The trigger rate of H.E.S.S.-I was between 200 and

300 Hz and this can lead to a substantial fraction of events not recorded in CT1–4, when they trigger in coincidence mode with CT5, which would imply losing about 30% of data or more [2].

The H.E.S.S.-I camera upgrade is centered on the redesign of the readout and control electronics of the camera. In the design of the new components, some concepts and technologies developed for CTA were used, thus the upgraded readout electronics is based on the NECTAr analog read sampler and digitizer chip [2]. The most delicate part of the upgraded electronics are the readout boards of the drawers, which were upgraded with a new analogue memory (NECTAr chip). The Photomultiplier Tubes (PMTs) and their bases that generate high voltage, which are the most expensive components of the array, were not upgraded.

The upgrade of the cameras also include the mechanical parts. The new ventilation system, mounted on the back door of the camera has been redesigned to steadily inject filtered and (optionally) heated air into the camera. The option to heat the incoming air can be used to get rid of humidity after periods of shutdown. The ventilation system allows to have a constant air flow through the drawers and all other openings of the camera and therefore allows for homogeneous cooling of the cameras [2, 3].

The first Cherenkov telescope of H.E.S.S.-I, CT1, was upgraded in July 2015, while the other three Cherenkov telescopes, CT2–4, were upgraded in September 2016. Full array observations might commence in spring 2017 [3].

3.2 H.E.S.S.-I cameras

The cameras of the H.E.S.S. telescopes serve to capture and record the Cherenkov images of air showers induced by very-high-energy gamma rays interacting in the upper atmosphere [1,2]. The cameras of the H.E.S.S. telescopes are based on the PMTs. These devices together with fast electronics allow for the detection of Cherenkov light coming from particle showers originated by very-high energy cosmic gamma rays interacting in the upper atmosphere [42]. A pixel consists of a PMT, with a Winston cone light collector capable of reducing the background contribution from albedo, i.e. stray light, by limiting the PMT's field of view to the angular size of the mirror [34]. In addition, the Winston cones fill the empty spaces in between neighbouring pixels.

Figure 3.2. The view of the front part of CT1 camera during the upgrade in 2015. When fully complete, this front part of the camera contains 60 interchangeable drawers, each with 16 PMTs lodged in a pigeon–hole plate.

Each camera consists of 960 pixels of 0.16° angular size providing a total field of view of 5° in diameter (about 10 times the diameter of the moon). Every PMT runs with high voltage, which is provided by a PMT base. The PMTs are calibrated to generate a signal of 2×10^5 electrons for every photoelectron. To achieve a large dynamic range, the pulse from each PMT is divided into a high gain channel and a low gain channel which have different amplification factors each. The design criteria of each camera includes a triggering scheme which allows to identify the brief and compact Cherenkov images and to reject backgrounds, such as the light of the night sky. The complete electronics for image digitization, readout and triggering is integrated into the camera body [2].

3.3 The trigger

H.E.S.S. has three levels of trigger. The first level acts between single pixels of a single telescope camera. The second one is the so called sector trigger, which acts on a group of pixels in the camera of a single telescope. The third one is the central trigger system, which is a multi-telescope coincidence trigger.

3.3.1 The camera trigger

The trigger scheme chosen for the upgraded camera is the same as for the current cameras [2]. During normal observations, a single pixel in the camera is triggered only if the number of photoelectrons detected reaches a certain threshold, typically 4 photoelectrons [29]. The camera array contains 38 overlapping trigger sectors, each one formed by 64 PMTs [34]. A sector will be triggered if the number of triggered single pixels in this sector exceeds a threshold, normally 3 to 5 pixels. This sector trigger is highly important for the reduction of the night sky background (NSB) because gamma ray induced air showers form images of clusters of pixels, while the photons of the NSB are randomly distributed over the whole camera.

3.3.2 The array trigger

For this trigger level, telescope multiplicity for the Cherenkov telescopes is selectable. Any local camera trigger signal starts the readout and simultaneously sends a message to the central system trigger electronics. The central system checks for coincidences of several telescope triggers within a certain time window and initiates the readout of the whole array or stops the readout of the triggered telescopes. At least a coincidence of two telescopes is required to get stereoscopic view of the same air shower. Also, a higher multiplicity increases the resolution of parameters like energy and shower direction. It also allows for the rejection of muons since muons can only trigger a single telescope [34].

3.4 The drawer

Each of the H.E.S.S-I camera contains 60 interchangeable drawers (see Fig. 3.3 for example) arranged in a 9×8 rectangular matrix, with each corner of the matrix free of three drawers [3]. The front-end readout electronics consisting of three electronics boards are organised in a drawer. Two of the electronics boards are the analog memory boards (see Fig. 3.4), and one slow control board.

The analog memory boards contain NECTAr chips where the signals from the PMTs routed. These analog memory boards are used for the acquisition, amplification, sampling, and digitization of the PMTs' signal.

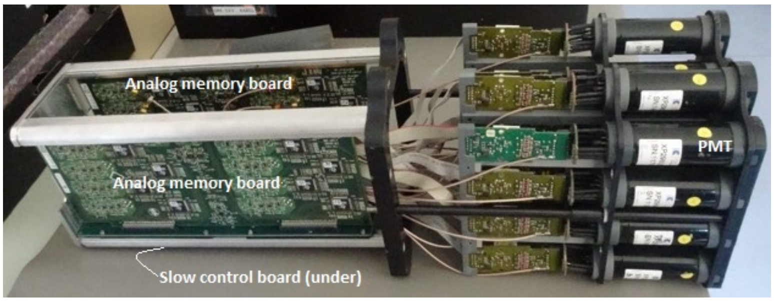

Figure 3.3. A complete drawer of the H.E.S.S.-I camera upgrade. The PMTs and their bases that generate high voltages are clearly visible.

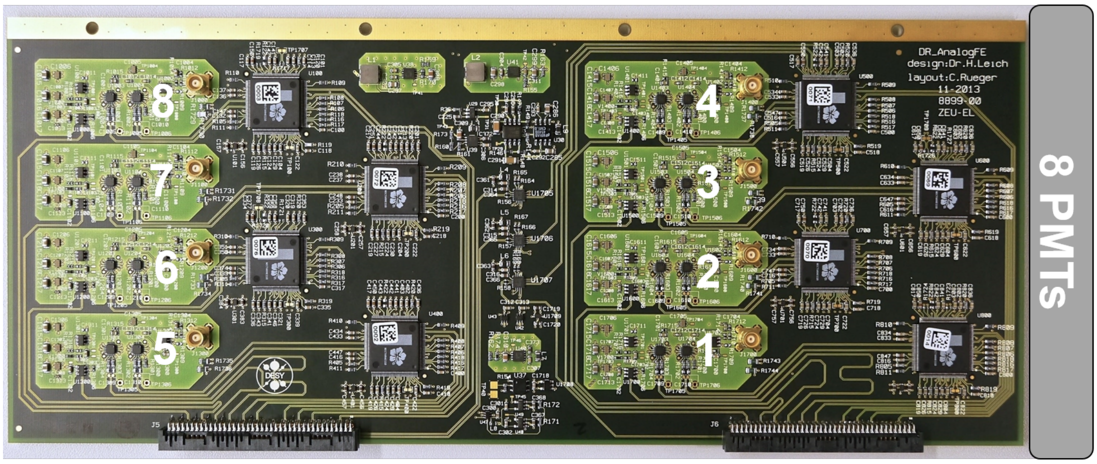

Figure 3.4. An analogue memory board of the H.E.S.S.-I camera upgrade. Each board hosts 8 NECTAr chips which are shown with the flower logo.

The slow control board is responsible for handling the the data stored by the analog memory boards and monitoring the PMTs. The Field Programmable Gate Array (FPGA) which reads out the digitized signals from the NECTAr chips and the ARM micro compter are located on the slow control board. The FPGA transits the digitized data to the ARM cpu, which buffers it and sends it to a central camera computer [2, 34]. Furthermore, the slow control board controls all the necessary settings of the data taking.

In short, the front-end readout electronics boards are responsible for processing and digitizing the PMTs' output signals before sending them to the Data Acquisition (DAQ) system [43].

3.4.1 The NECTAr chip

If a photon enters a PMT, the photo effect converts it into an electron, which is then multiplied by the dynodes, using the high voltage. The resulting PMT signal is terminated with a resistance $R = 50\ \Omega$, pre-amplified, split into three branches that are further amplified [2]. One of the three signal branches is amplified by a factor 45 and routed to a comparator, of which its output goes directly to the FPGA where it is sampled at 800 MHz and is used to generate the trigger. The other two branches are used for data acquisition, with two different gains: the high gain (HG) and low gain (LG) branches which are routed to a NECTAr chip. The HG branch is designed for low intensity signals and the LG branch is for high intensity signals in each chip. The two gains, LG and HG have amplification factors of 15.1 and 0.68 respectively [2, 3]. Operations are simultaneous on the 2 branches that are used to sample the low and high gain signals of a PMT.

The high HG branch is used to detect signal charges from 0 up to 200 photoelectrons (p.e.). The LG branch is used to cover the range from 30 to 4125 p.e. The linear range used for analysis for both branches is shown in Fig. 3.6 [3].

Each input signal (analogue voltage) from the PMT is routed to the NECTAr chip, where it is continuously sampled at a rate of 1 GS/s (giga samples per second) and stored in successive cells of a bank of 1024 capacitors (ring buffer), arranged in a matrix of 16 lines of 64 cells each [44]. Each storage cell in a ring buffer is 1 ns long. In normal operations only a small fraction of the cells inside a region that correspond to the duration of the Cherenkov light (usually 16 cells long) are read out.

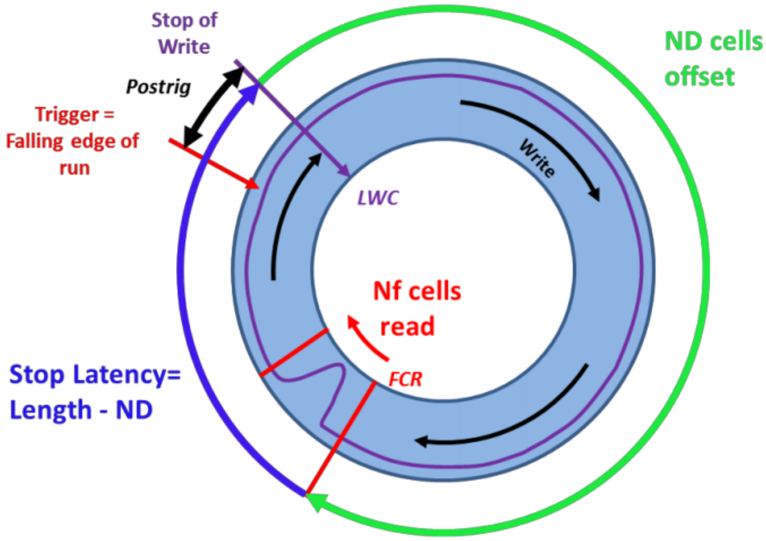

Figure 3.5. The working principle of a NECTAr chip [44]. The length of the Cherenkov signal is N_f ns. Since the readout window, N_f, has to be as small as possible to reduce the contamination of a signal with night sky background and electronic noise, the N_f value is set to 16 ns, which is enough to contain the Cherenkov signal.

Fig. 3.5 shows how the NECTAr chip operates. If a trigger signal is received, the writing process is stopped and N_f samples of the ring buffer are digitized by a 12-bit 21 MHz Analogue-to-Digital Converter (ADC) and converted into charge equivalent ADC counts, starting at a programmable readout offset N_d [3,44]. The readout samples start from the cell with an index FCR (First Cell to Read), where each 1 ns segment of the time period N_f is read out separately. The digitized signals are then stored and processed in the FPGA. An ARM-based embedded linux computer reads out the FPGA and forms the events that are then sent to a central computer for further processing [3]. The N_f samples are summed to give two ADC values per pixel (HG and LG) which can be used for analysis and, eventually, for geometric shower reconstruction.

3.5 Calibration of the H.E.S.S. cameras

In order to reconstruct the properties of a primary gamma ray, calibration procedures have to be applied to the raw images acquired by the H.E.S.S. cameras (the image will typically look as in Fig. 2.6). Such a raw images consist of two values per pixel, the HG and LG, given in ADC counts. Section 3.5.1 describes the standard calibration of the H.E.S.S. data and how this method is used to turn the raw data into intensities of photoelectrons from Cherenkov photons.

3.5.1 Converting ADC values to photo electron intensities

The calibration of the data involves the conversion of the ADC counts of a given pixel to a corrected pixel intensity in photo electrons. The signal amplitude of each pixel is the starting point for the standard Cherenkov image analysis. This amplitude is the charge in photoelectrons induced by Cherenkov light on the PMT. The calibration provides the required conversion coefficients from ADC counts to corrected photoelectrons. For each event, ADC counts are measured for the HG and LG branch in each pixel. The amplitudes in photoelectrons for every pixel are calculated as follows: [45]

$$A^{HG} = \frac{ADC^{HG} - P^{HG}}{\gamma_e^{ADC}} \times FF \quad (3.1)$$

$$A^{LG} = \frac{ADC^{LG} - P^{LG}}{\gamma_e^{ADC}} \times (HG/LG) \times FF \quad (3.2)$$

In these formulae:

- A^{HG} and A^{LG} are the amplitudes in Cherenkov photoelectrons to be determined for the high and low gain branches respectively,
- ADC^{HG} and ADC^{LG} are the ADC counts measured in the high and low gain branches of the pixel,
- P^{HG} and P^{LG} are the ADC pedestal positions of the baseline for both branches. i.e. the values corresponding to zero photoelectrons from Cherenkov light,
- γ_e^{ADC} is the gain of the high gain branch in ADC counts per photoelectron (after pedestal subtraction),
- HG/LG is the amplification ratio of the high gain to the low gain branch. This is needed because the gain factor γ_e^{ADC} is calculated only for the high gain branch,
- and FF is the flat-field coefficient, used to correct for different optical and quantum efficiencies between pixels within a camera.

The A^{HG} and A^{LG} are both used in image analysis to provide a single pixel amplitude, provided that both gain branches function properly. It is also essential that any non-operational pixels or pixel branches are identified in the calibration process in order to avoid miscalculation of amplitudes. If for a single pixel both channels work properly, the high gain value A^{HG} is used up to ≈200 p.e. and the low gain value for values above ≈4125 p.e. (see Fig. 3.6) [3]. For intermediate values, a weighted average of the two amplitudes is used:

$$A = (1 - \epsilon) \cdot ADC^{HG} + \epsilon \cdot ADC^{LG}, \qquad 0 \leq \epsilon \leq 1 \tag{3.3}$$

where $\epsilon = (A^{HG} - 200 \text{ p.e.})/(4124 \text{ p.e.} - 200 \text{ p.e.})$ [3, 45]

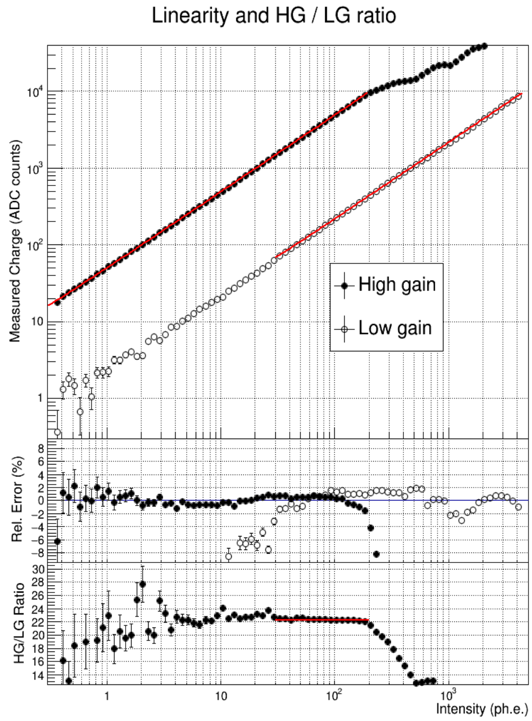

Figure 3.6. Summary of the linearity results for a typical channel of the upgrade. In the top frame, response curves are shown of both HG (filled circles) and LG (empty circles) of the readout channels. The linear range is about 200 ph.e. for HG, and 4125 ph.e. for LG [3].

3.5.2 Pedestal estimation

For a given channel, the pedestal is defined by the value of the signal in ADC counts recorded with no Cherenkov light. Pedestal positions (P^{HG} and P^{LG}) are obtained by calculating the mean value of the ADC counts distribution per channel. The shape of pedestal (charge distribution) depends on the noise in the camera electronics, level of night sky background and temperature. The mean pedestal position therefore corresponds to the position in ADC counts of zero photoelectrons of Cherenkov light.

During data taking, about $\mathcal{O}(10)$ pixels of each camera are contaminated by Cherenkov light, thus the rest of the pixels can be used to determine the pedestal positions. Since pedestals depend on temperature,they are determined during observation runs as often as possible, approximately every minute to minimise the impact of pedestal drift due to temperature variations in the electronics.

3.5.3 The gain factor

The gain factor γ_e^{ADC}, or the ADC to photoelectron coefficient, of a given pixel is a measure of the number of ADC counts above pedestal value which corresponds to one photoelectron. It can be obtained from dedicated runs, called single photoelectron run, taken frequently during each observation period. In such runs, the pixels are illuminated with a weak light source to create single photoelectron signals, see Fig. 3.7. The γ_e^{ADC} coefficient is only calculated for the HG branch of the pixel, as for the case of the LG branch the single p.e. peak cannot be resolved as it is shifted into the pedestal peak [30, 45, 46].

Fig. 3.7 shows the results of a PMT gain calibration of the upgrade. To extract a γ_e^{ADC} coefficient, a fit (solid line) was applied with the following assumptions. The distribution consists of a Gaussian pedestal peak and additional peaks for 1, 2, 3, ..., n p.e. signals, which all are described by a Gaussian too. Furthermore, the number n of photoelectrons is assumed to follow a Poisson distribution.

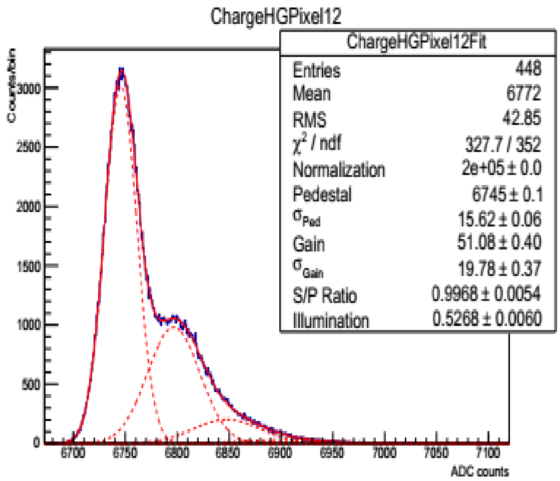

Figure 3.7. ADC distribution of a single photo electron illumination of a photomultiplier for the HighGain channel. The large peak is the pedestal peak, the second peak and its tail are due to the 1, 2, 3, ..., n photoelectrons signals. Figure taken from [3].

3.5.4 The amplification ratio between the HG and LG branches

As already mentioned in subsection 3.5.3, no gain factor is determined for the LG branch of the pixel. Instead, the amplification ratio between the HG and LG branches is measured using events from normal observation runs. Since for each pixel, the LG and HG branches are only comparable in their overlapping linear range of operation, the intensity of a pixel has to be between 80 p.e. and 200 p.e., see Fig. 3.6, to be used for this calculation (Eq. 3.2).

3.5.5 Flat-field coefficients

Different photocathode efficiencies and different Winston cone light collection efficiencies produce some inhomogeneity in the camera. The flat-field coefficients (FF) are used to correct for these differences. The flat-field coefficients are determined from dedicated flat-field runs (taken roughly every 2 days) which use LED flashers mounted on the telescope dishes at 15 m from the cameras to provide uniform illumination [45]. For each event the mean signal over each camera is calculated, excluding unusable pixels (malfunctioned pixels) and the ratio of the pixel intensity to the camera mean is stored in a histogram. The mean of this distribution is the efficiency of the pixel relative to the camera mean and the inverse value is used as the flat-field coefficient which is used to correct for pixel efficiency difference [24, 45, 46].

Once the data from an event has been processed as described above, further analysis of the camera images is possible, including the parametrisation of shower geometries and the reconstruction of the direction of the primary photon.

3.6 Cross-talk between pixels

When a PMT detects Cherenkov photons from an atmospheric shower, it generates an electrical pulse of current, which is routed to the NECTAr chip on the analogue board [3]. This flow of electrical charge creates changing magnetic fields. When these magnetic fields cut across the neighbouring channels on the analog board, voltages are induced into them. This voltage in the neighbouring channels of the readout boards is the cross-talk. In short, the cross-talk is the undesirable exchange of signals between closely spaced electrical elements (channels).

The following procedure was used to measure the cross-talk between the pixels: An Agilent Technologies 81160A arbitrary pulse generator was used to generate pulses that were routed individually to all 16 channels of one drawer, one by one, and the attenuation factors from 0 to 81dB (with 1 attenuation step) were applied.

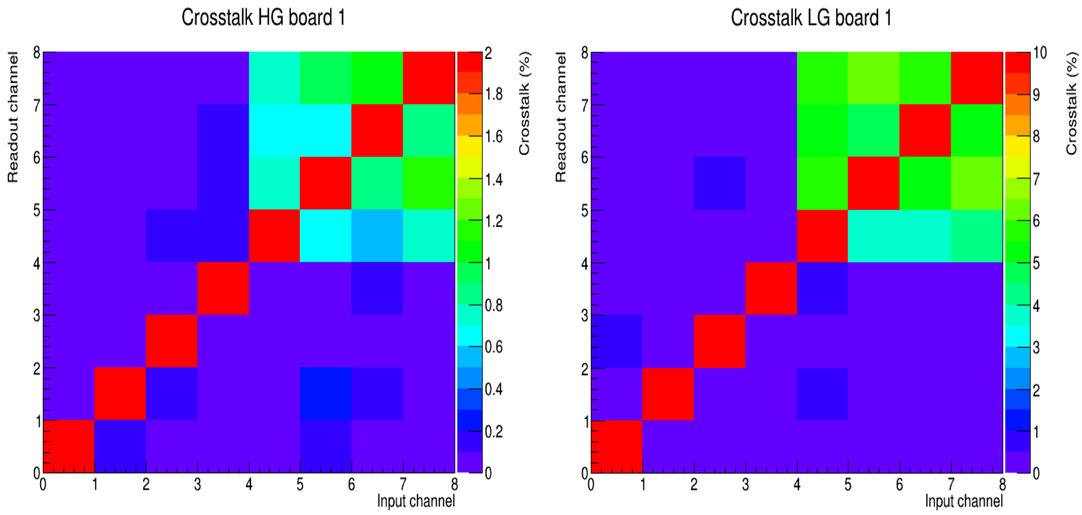

Figure 3.8. The cross-talk matrix for a readout board (like Fig. 3.4) of the upgrade. On the left is the cross-talk in high gain and on the right is the cross-talk for the low gain of the same analog readout board.

Fig. 3.8 shows the cross-talk between the pixels in an analog board of a drawer for both LG and HG branches. The x-axes represent the input channel, and the y-axes are the readout channels. The colorscale indicates the strength of the cross-talk. The high cross-talk in channel 5–8 in high gain and low gain branches is evident in Fig. 3.8. The cross-talk evident in Fig. 3.8 is less than 2% in high gain and less than 10% in low gain.

Chapter 4

The aim of the study

As already mentioned in the introduction, the aim of this study was understand the origin of the significant level of the cross-talk observed in the front-end analog readout boards of the H.E.S.S-I camera upgrade. The level of cross-talk is more than expected in the rear part of the readout board compared to the front part of the same readout board (see Fig. 3.8). The observation of such level of cross-talk for the channel 5–8 motivated a deeper study of the pedestals of the electronics of the upgraded H.E.S.S.-I cameras, since the cameras require a low level of noise in their electronics in order to capture the faint light and individual Cherenkov photons. Also, a low level of noise in the camera electronics improves the accuracy in the interpretation of the data which in turn leads to better results from the data taken with these cameras.

Electronic pedestals were chosen to study the the noise level (pedestal width) since in this case, only electronic noise is readout and this may allow for identification of the source of noise in the analog readout electronics.

Chapter 5

Materials and methods

A full copy of H.E.S.S.-I cameras was produced for testing new camera electronics of the upgrade at DESY in Zeuthen, Germany. About 270 drawers were produced and tested for the upgrade. The dark box with a mini camera that can accommodate 4 drawers per test was also constructed to create a realistic dark trigger. A copy of the H.E.S.S. DAQ was also attached to this mini camera and the original state transitions of the system were emulated [3].

The electronic pedestals data were taken with a drawer on the Test bench at DESY. To measure the electronic pedestals, no light pulses were sent to the PMTs, the high voltage was enabled, and signals were recorded using an internal trigger. 16 Samples containing the pedestal were readout and saved into a text file for each channel (pixel). 1000 events were recorded for each channel in a drawer, and thus providing satisfactory statistics. A C++ code written in ROOT modular scientific software framework was developed for the analysis of the data.

5.1 Electronic pedestals

The first step towards the statistical study of electronic pedestals was to obtain the electronic pedestal waveform. Electronic pedestals is the signal recorded when there is no light at all coming to a PMT, i.e. only electronic noise is read out. This noise must be accounted for because it generates additional charges that can modify the output waveform of a signal produced by Cherenkov photons hitting the PMT.

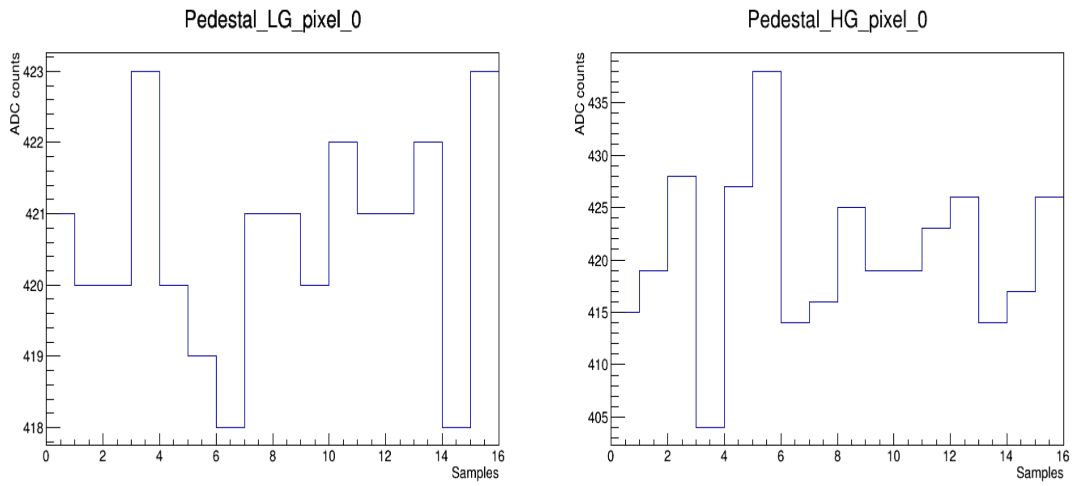

Figure 5.1. Electronic pedestals waveform for channel 1. On the left is the low gain and right is high gain of the same PMT channel. Each sample on the x-axis is 1 ns wide.

Fig. 5.1 shows the waveform (time distribution of a single event as function of the samples) of electronic pedestals of channel 1 of the analog readout board. The waveforms show oscillations around the mean value, called the pedestal position (mean: 420.63 ADC counts, RMS of the distribution: 1.750 ADC counts for low gain and mean: 420.63 ADC counts, RMS: 7.82 ADC counts for the high gain branch). The samples on the x-axes correspond to a time window of 16 ns, N_f in Fig. 3.5, which is bigger than the duration of the signal coming from Cherenkov light, typically ∼10 ns.

Following the fact that the significant level of cross-talk has been observed for channels 5–8 as shown in Fig. 3.8, only plots for two channels of the analog readout board will be shown afterwards in this thesis. For comparison sake, one plot will represent the left side of Fig. 3.4 (channel 1–4) which has *more* noise, and one from the right side of Fig. 3.4 (channel 5–8) which has *less* noise. All other plots will be shown at the end of the thesis in the appendices.

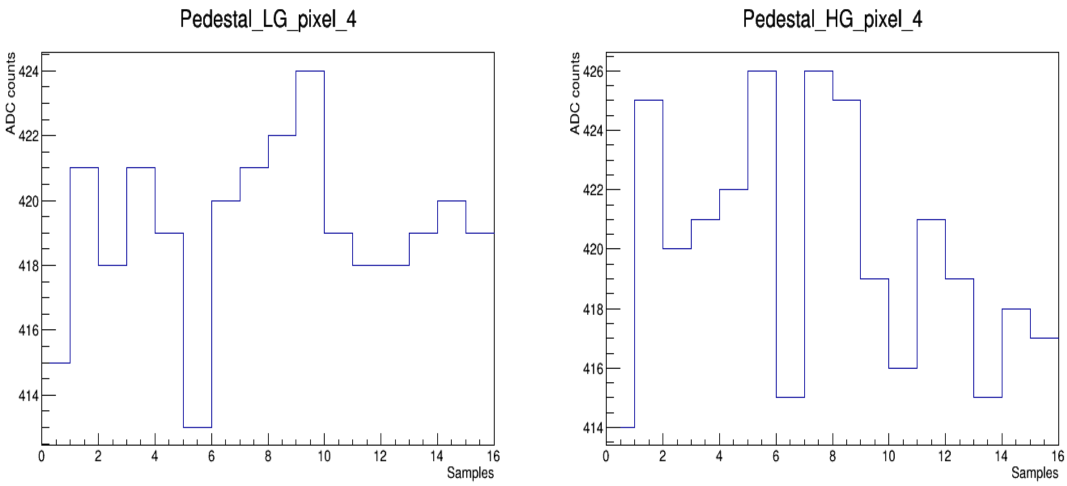

Figure 5.2. Electronic pedestals waveform for channel 5. On the left is the low gain and right is high gain of the same PMT channel. The number 4 in the title of each sub-figure is due to the fact that C++ starts indexing at zero.

Fig. 5.2 shows the electronic pedestals of channel 5 which is one of the channel in the noisy part of the readout board. The mean values for the pedestals are 419.19 ADC counts in LG and 419.94 ADC counts in HG of the same PMT channel. The RMSes of the distribution are 2.61 ADC counts in LG and 4.04 ADC counts in HG.

In the following sections, analysis methods used to analyze electronic pedestals are described in details. All results for the analysis methods described here are shown in chapter 6.

5.2 The autocorrelation function

Very often, it is difficult to judge if data in a waveform is random or periodic, the autocorrelation function (ACF) will help here. The autocorrelation function characterizes the correlation of a signal with itself. It is a convolution of the signal function with itself. The autocorrelation function tells us the time interval over which a correlation in the signal exists [47].

For a discrete signal, *y(t)*, the autocorrelation coefficient C at lag n can be defined as:

$$C(n) = \frac{1}{N} \sum_{k=i}^{i+n-1} y(k)y(k-n) \tag{5.1}$$

Where N is the total number of samples of the signal function, *y(t)*, over which the coefficients are calculated and $i, k, n \,\epsilon\, \mathbb{Z}$ [48].

The process:

The ACF tells how correlated point are with each other based on how many time steps they are separated by. This is done by taking two copies of the signal, and moving one forward by one sample. The two copies are then multiplied together, and all the values are added up. This is repeated for two samples difference and so on, up to the number of samples in the signal. This gives a small result if the data in the waveform is random (for example, noise) and a large result if the data is repetitive.

The autocorrelation coefficient, ACF(0), gives the highest peak on a graph when all data are perfectly correlated with themselves. If, for any larger values of lag n, the autocorrelation coefficient of exactly ACF(0) is obtained, then the signal delayed by a time n is identical to the signal with no delay. In that case the signal must be periodic.

When the correlation is normalised, its magnitude will range from 0 to 1. If the correlation coefficients are close to zero, the signal will be considered not to keep its linear relation increasing the distance between two points, in this case the data is random.

5.3 The Discrete Fourier Transform

The Fourier transform is a mathematical method for transforming a function of time into a function of frequency, i.e. it is an algorithm that takes a signal and determines the frequency content of the signal. The DFT operates on a sampled time domain signal which is periodic. The DFT of a one-dimensional function $y(t)$ of length N can be defined as follows [49]:

$$Y_k = \sum_{n=0}^{N-1} y_n e^{-2\pi ikn/N} \tag{5.2}$$

Equation 5.2 allows the transfer from the time domain to the frequency domain where y_n is the n$^{\text{th}}$ element of input sampled signal in time domain, and Y_k is the k$^{\text{th}}$ element of output sequence in frequency domain. N is the number of samples of the signal y, $i = \sqrt{-1}$, while $k, n \in \mathbb{Z}$, for $n, k = 0, 1, 2, \ldots N\text{-}1$.

Equation 5.2 looks very similar to the correlation equation described earlier in section 5.2 because it is calculating the correlation between a signal $y(n)$ and a function $e^{-2\pi ikn/N}$. But what does it really mean for a signal to be similar to a complex exponential? To see that, it makes sense to break the exponent into sine and cosine components.

Let the exponent in equation 5.2 be $\theta = -2\pi kn/N$. Then using Euler's formula for complex numbers: $e^{i\theta} = \cos(\theta) + i\sin(\theta)$, and two properties of sines and cosines: $\cos(-\theta) = \cos(\theta)$ and $\sin(-\theta) = -\sin(\theta)$, equation 5.2 can be rewritten as:

$$
\begin{aligned}
Y_k &= \sum_{n=0}^{N-1} y_n(\cos(\theta) + i\sin(\theta)) \\
&= \sum_{n=0}^{N-1} y_n(\cos(2\pi kn/N) - i\sin(2\pi kn/N))
\end{aligned} \tag{5.3}
$$

Equation 5.3 shows that a function y can be broken down into its constituent frequencies (i.e. into sines and cosines of all frequencies) which contribute to the signal. More important, the equation also tells the amplitude of the waves present in the signal y, which correspond to their intensity levels.

5.3.1 The Fast Fourier Transform

The fast Fourier transform (FFT) is a fast algorithm used to compute the DFT of a signal. Using the FFT instead of DFT reduces the computational complexity from $\mathcal{O}(N^2)$ to $\mathcal{O}$(N log N) [49]. Therefore, the results of a FFT is simply equal to that of a DFT performed on the same input. The FFT becomes more preferable over the DFT as the number of samples N in the signal increase. For this reason, the FFT is used in this project.

5.3.2 Sampling theorem

Let the sinal function *y(t)* be sampled at evenly spaced intervals in time. Let Δ denotes the time interval between consecutive samples, so that the sequence sampled is

$$
y_n = y_n(n\Delta) \qquad\qquad n = ..., -3, -2, -1, 0, 1, 2, 3, ... \tag{5.4}
$$

The reciprocal of the time interval Δ is called the *sampling rate* f_s. For any sampling interval Δ, there is a special frequency f_c, called the *Nyquist critical frequency*, given by

$$f_c \equiv \frac{1}{2\Delta} \tag{5.5}$$

The Nyquist frequency f_s is the highest frequency contained in the signal according to the sampling theorem [49]. If for instance the time interval is 1 ns, then the Nyquist frequency is $f_s = \frac{1}{2 \cdot 10^{-9}\ \mathrm{s}} = 500$ MHz. Since the spectrum for the FFT is mirrored (in this case at 500 MHz), the first half of N/2 bins contain all necessary information on the spectrum, the second half can be discarded.

Chapter 6

Results and discussion

In this chapter, the results from analysis methods described in chapter 5 are presented.

6.1 Autocorrelation

The plots of correlation coefficients from the autocorrelation versus the delay (time lag) of the signal from channel 1 are shown in Fig. 6.1 for both low and high gain respectively. For better visibility, the correlation coefficients were calculated with lag n ranging from 0 up to 20.

As mentioned in section 5.2, the autocorrelation function gives a peak at a point where the two signals are most similar. In Fig. 6.1, the highest peak for the correlation is achieved at lag $n = 0$ and 16 in both high and low gain. The peak at $n = 16$ arises due to the fact that the coefficients were computed up to $n = 16$, thus an *artificial periodicity* of 16 samples appears since the signal is 16-samples long.

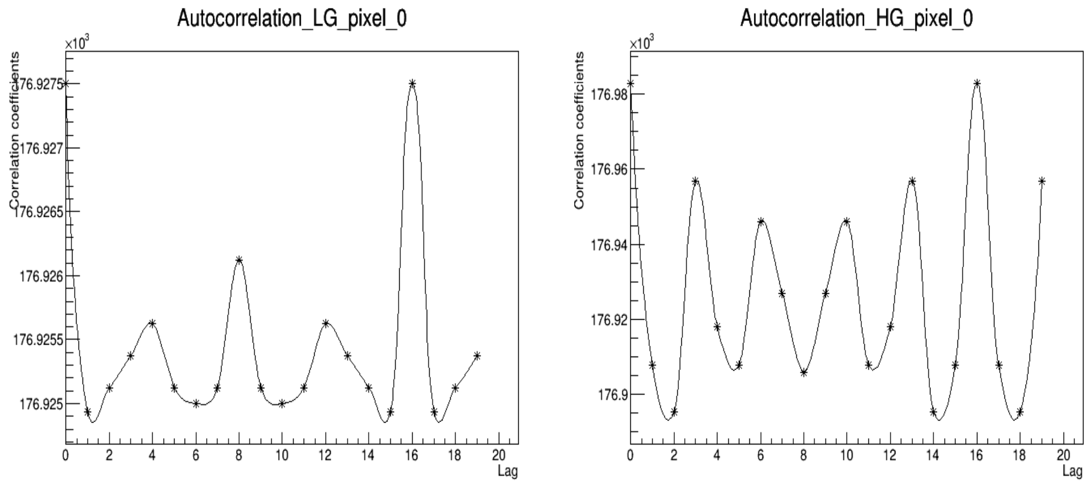

Figure 6.1. Autocorrelation of the waveforms in Fig 5.1.

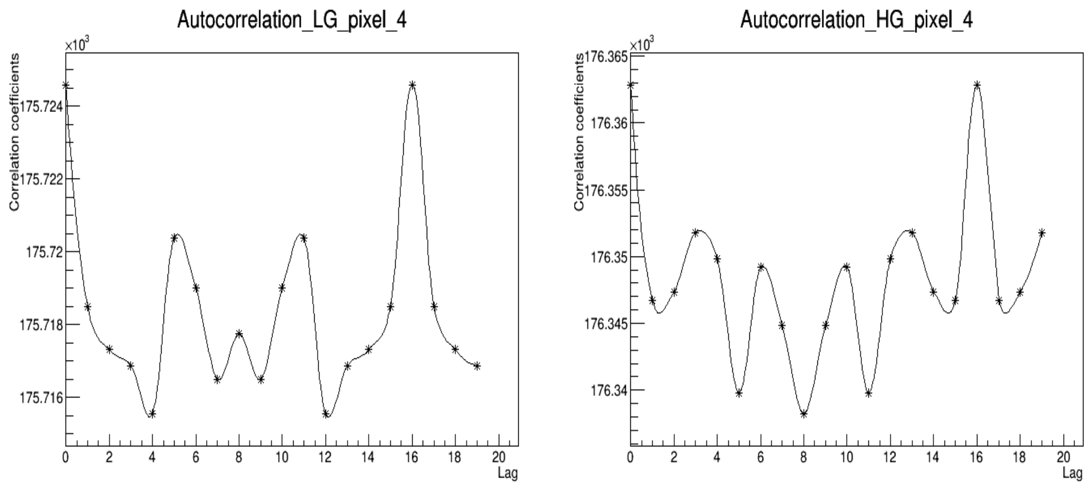

Figure 6.2. Autocorrelation of the waveforms in Fig 5.2.

As with pedestals, the autocorrelation function was computed for all 16 channels of the drawer. Again as a reminder, channel 1 is on the region of the analog readout board with *less* noise. It should be noted that Fig. 6.1 is a plot of a single event. To compare the two regions of the analog board, Fig. 6.2, which is also a single event plot, is shown which is from a region of the same analog readout board with *more* noise. Fig. 6.2 looks pretty different from Fig. 6.1 which is not surprising because Fig. 6.2 is for the channels from a region with high noise level, thus random peaks are evident.

So far, what have been shown is the correlation for a single event. In order to make an educated conclusion about the results, it was necessary to take 1000 pedestal events and to compute the correlation for 1000 events piled up, to see if on a long term certain feature(s) would show up.

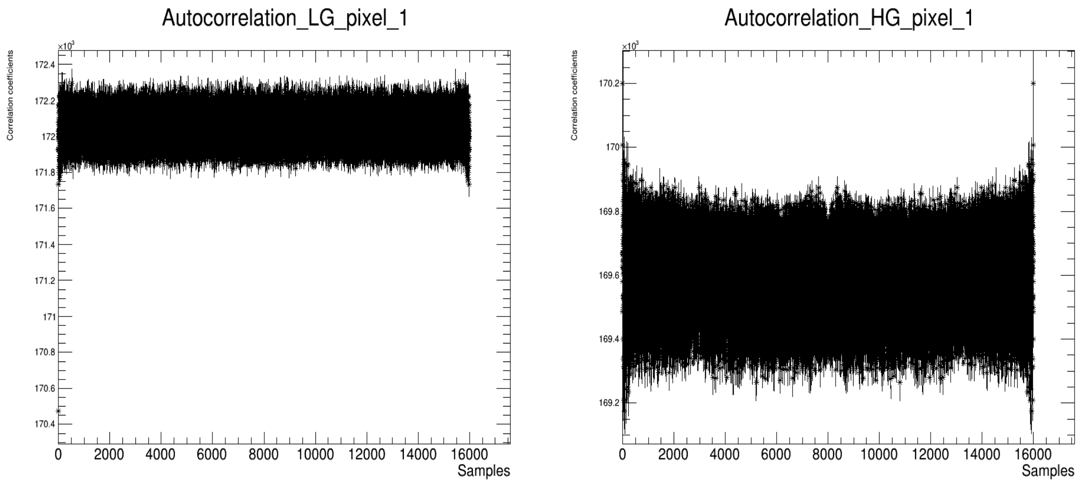

Figure 6.3. Autocorrelation for a 1000 events for pixel 1.

Fig. 6.3 and Fig. 6.4 look similar to Fig. 6.1 and Fig. 6.2.

From the computation of the autocorrelation function, also with a 1000 events, there is no observed correlation when the signals are projected along themselves for all channels. However, due to random noise the values of the correlation coefficients vary from channel to channel in both gains of the readout boards.

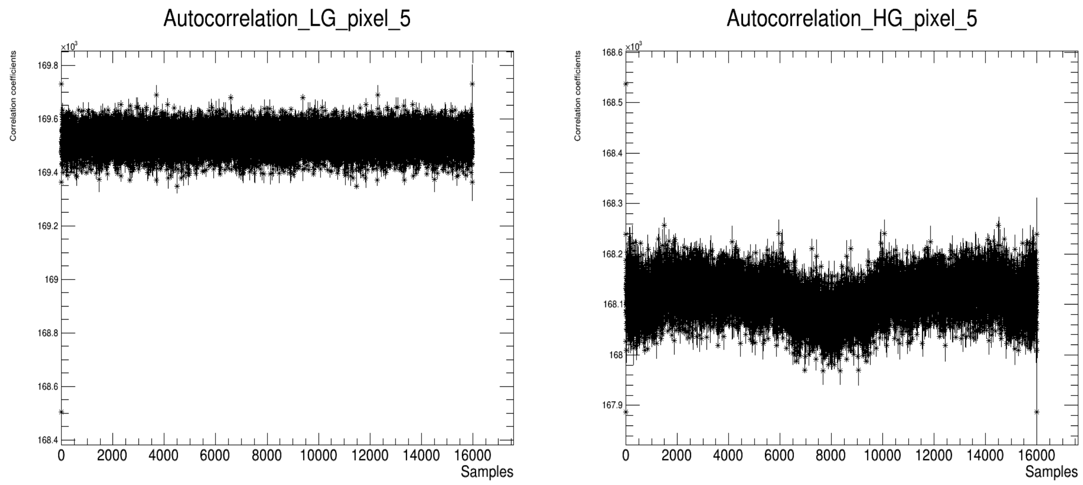

Figure 6.4. Autocorrelation for a 1000 events for pixel 5.

6.2 Pixel to pixel correlation

Here, the correlation between 2 pixels is computed at the same distance of the PMTs, to see if there exists a correlation between the pixels for example 1,2,3,4 and 5,6,7,8. It is the same as the autocorrelation, except that instead of searching for correlations inside the waveform of one pixel, the correlation is computed between two waveforms from two different pixels.

Fig. 6.5 shows the correlation between channel 1 and 5 of analog readout board 1 of the drawer. The peaks visible are random.

Fig. 6.6 shows the correlation between channel 9 and channel 13 of board 2 of the drawer. The peaks visible are also random, hence there exists no correlation between the two different channels of the same readout board. The same is true for all 16 channels in a drawer, (see appendix C).

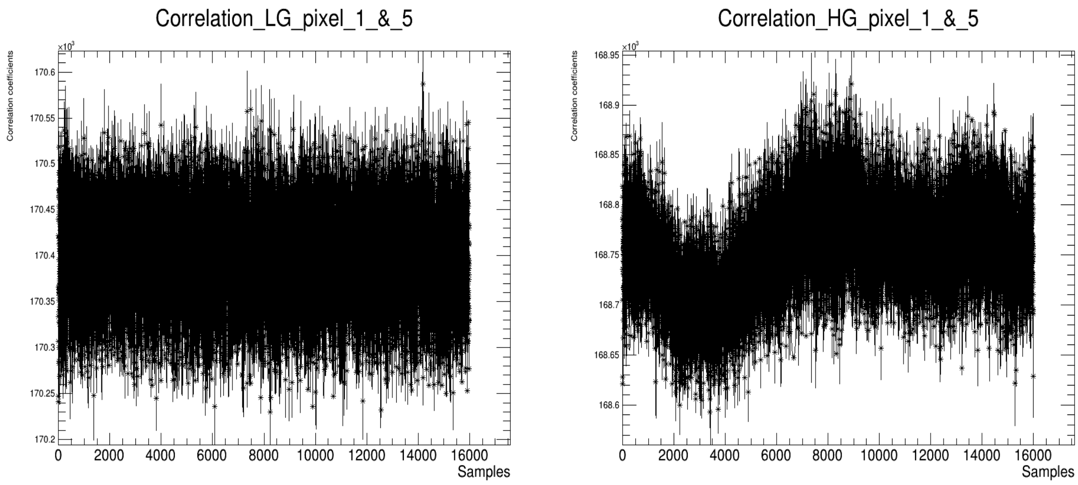

Figure 6.5. Correlation between two pixels, pixel 1 and 5 of board 1 of the drawer. On the left is the correlation between the low gain branches of pixel 1 and 5, and on the right is the correlation between the high gain branches of the same pixels.

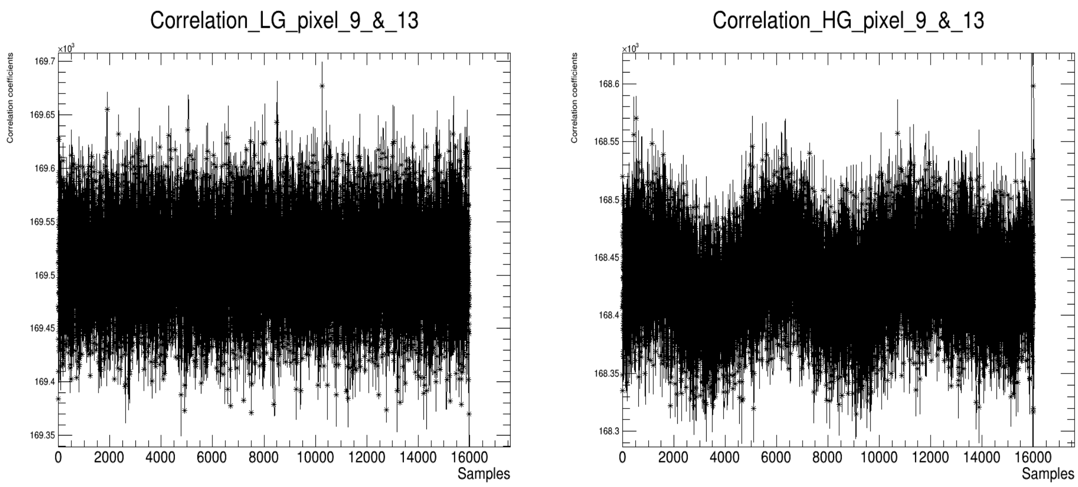

Figure 6.6. Correlation between two pixels, pixel 9 and 13 of board 2 of the drawer. On the left is the correlation between the low gain branches of pixel 9 and 13, and on the right is the correlation between the high gain branches of the same pixels.

6.3 Mean and RMS distributions

6.3.1 Mean distribution

Fig 6.7 show the distribution of the mean of 1000 events of electronic pedestals in the LG and HG branches of channel 1. Electronic noise creates a narrow Gaussian ADC counts distribution, the mean of which is the so called electronic pedestal position. The electronic intrinsic noise is the width of the pedestal peak, and it is about 4 ADC counts for the LG and about 5 ADC counts for the HG branch of the same channel.

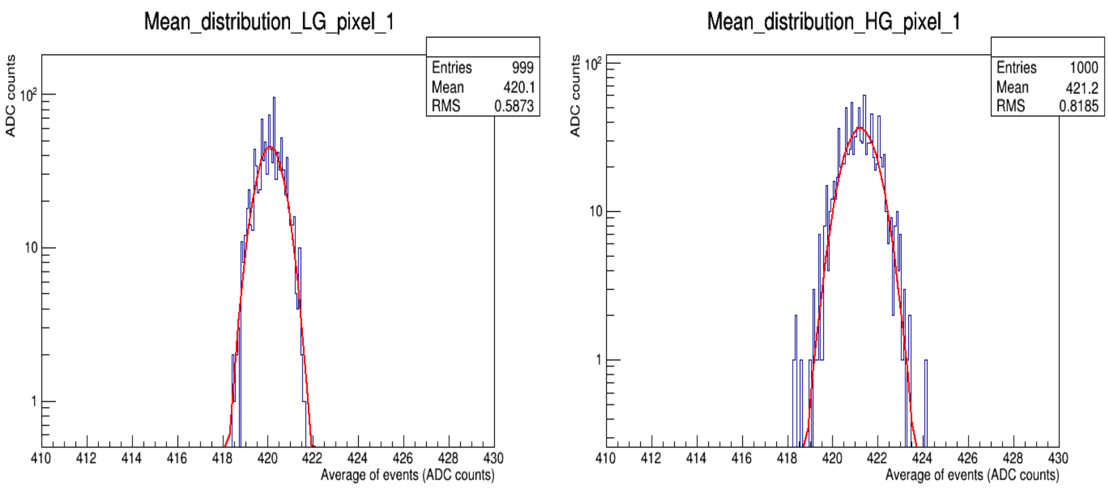

Figure 6.7. Distribution of the mean events of electronic pedestals of channel 1. The distribution of the mean is shown by a blue line, and the Gaussian fit is plotted in red.

Fig. 6.8 shows the distribution of the mean of the pedestals in the region of board 1 that has *more* noise. The width of the distribution is about 5 ADC counts in the LG branch and about 7 ADC counts in the HG branch of channel 5. The distribution of the means is Gaussian as expected.

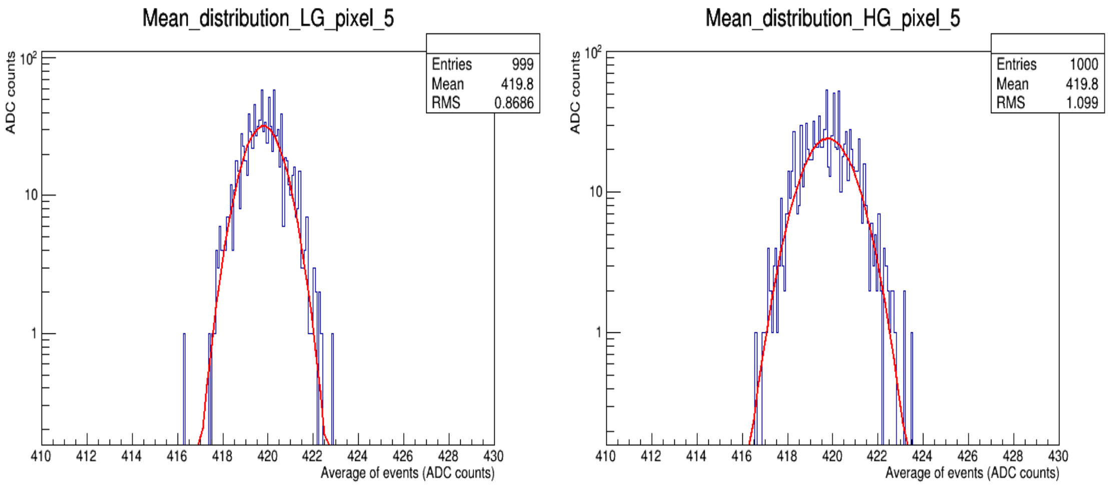

Figure 6.8. Distribution of the mean events of electronic pedestals of channel 5.

6.3.2 RMS distribution

The distribution of the pedestal noise (RMS) is shown here. The RMSes were computed from individual events. In Fig. 6.9, in the LG branch, the distribution is very Gaussian, however, on in the HG branch distribution does not resemble a Gaussian. This suggests that there is more noise in the HG branch of the pixel.

In the region of the readout board that has *more* noise, Fig. 6.10, it can be clearly seen that the distribution is not Gaussian as it supposed to be, but a bimodal distribution, especially in the HG branches of the drawer.

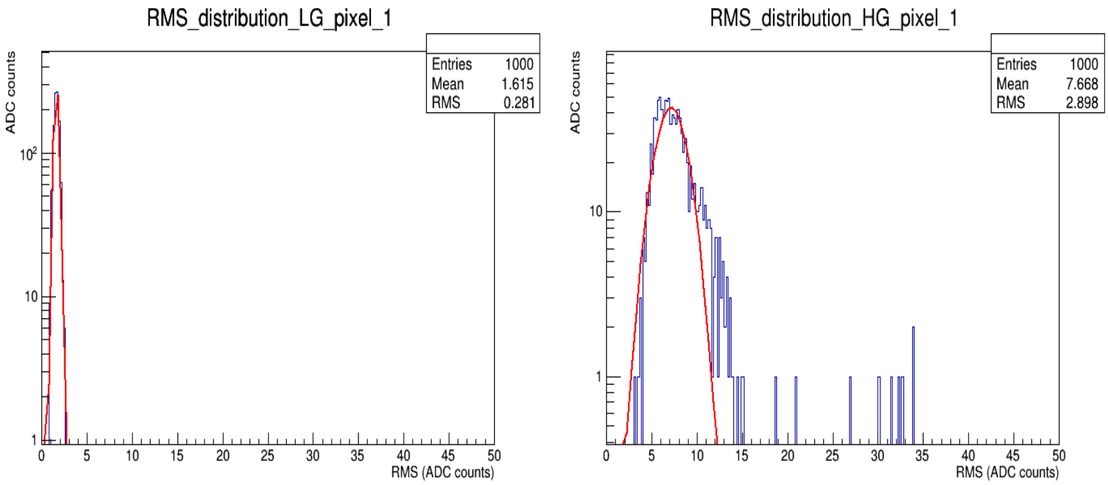

Figure 6.9. Distribution of the RMS of 1000 electronic pedestals events of channel 1. The blue histogram shows the distribution of the RMS, and the red line corresponds to a Gaussian fit. One can see outliers on the right of the fit in the RMS distribution of the high gain branch.

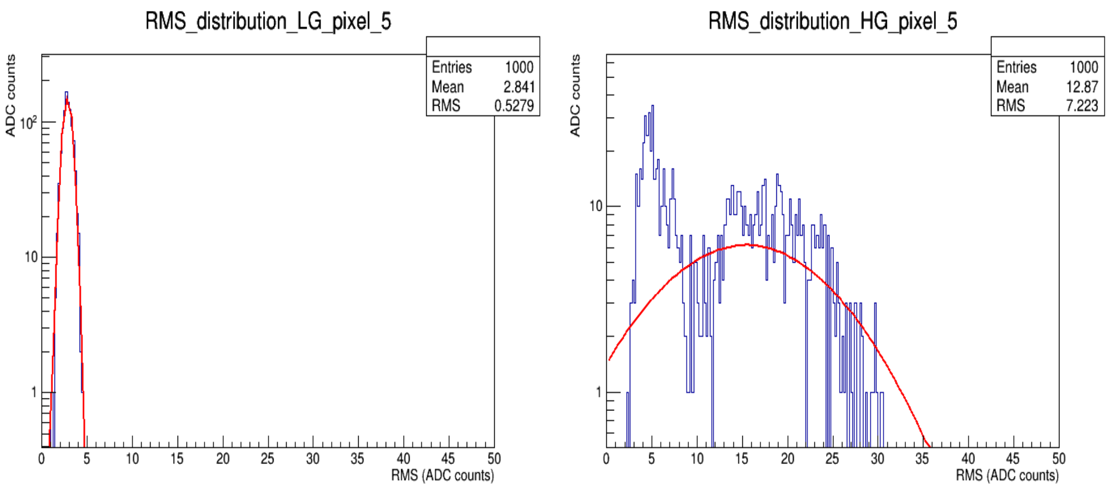

Figure 6.10. Distribution of the RMS of 1000 electronic pedestals events of channel 5.

6.4 Fourier transform

The Fourier transform was computed for all channels in a drawer, however, the results shown here are only for two channels of the analog readout board of the drawer. For full results on the Fourier transform of the drawer, see appendix F.

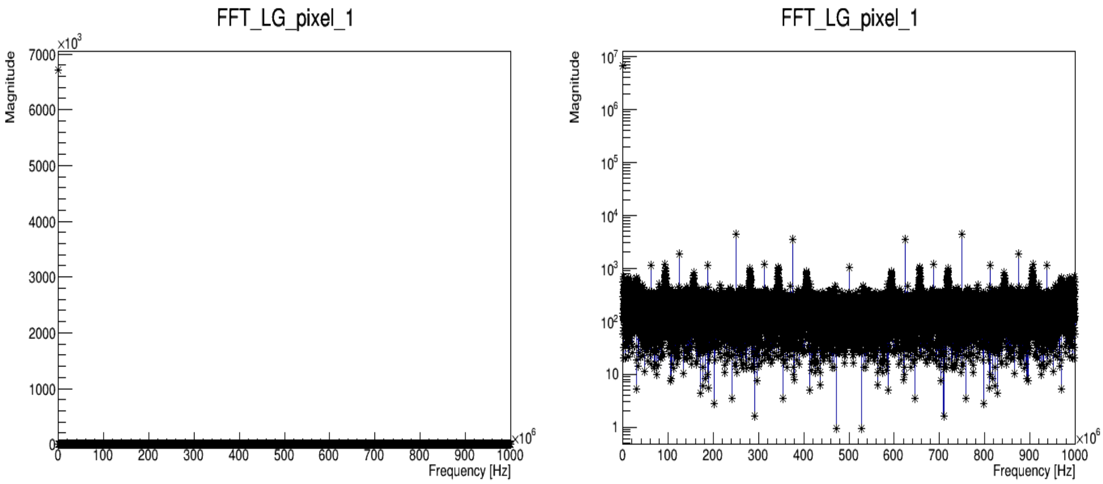

Figure 6.11. The Fourier transform for pixel 1 in the LG branch of board 1. On the right is the same plot plotted in logarithmic scale. Note the prominent peak on the y-axis of the transform, the DC offset which carries no frequency dependent information and hence can be ignored.

Fig. 6.11 and Fig. 6.12 show the Fourier transform of the signal sampled from channel 1. The y-axes show the magnitude of the waves contained in the signal. The magnitude tells the strength of the frequency components relative to other components. The magnitudes can be calculated using the following formula:

$$magnitude = \sqrt{(realpart)^2 + (imaginarypart)^2} \tag{6.1}$$

where the real and imaginary parts are from equation 5.3.

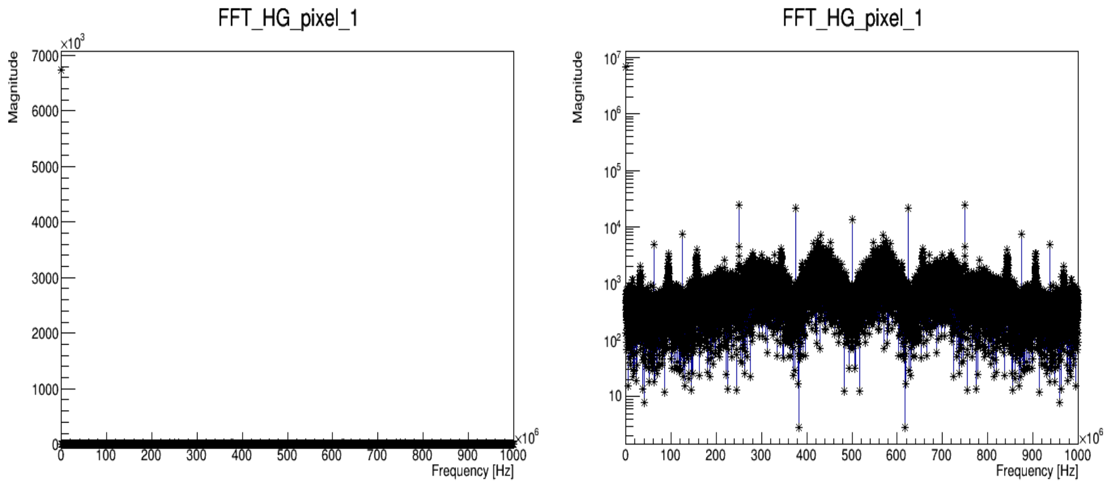

Figure 6.12. The Fourier transform of pixel 1 (with *less* noise) for a 1000 events in the HG branch of board 1. On the right is the same plot plotted in logarithmic scale.

The sampling frequency is plotted on the x-axes. The first peaks in Fig. 6.11 and Fig. 6.12 are the amplitude with zero frequency and it is equivalent to the sum of all the samples in the window.

There are no other peaks visible on the linear scale except the zero frequency peak , however, in logarithmic scale, the Fourier transform shows that now the spectrum contains many minor frequencies that one can even see the relative difference in their intensities.

As already mentioned in subsection 5.3.2, the spectrum is mirrored at 500 MHz, hence only information until 500 MHz on the x-axes of the Fourier transforms shown here must be considered useful. So that is for each actual frequency in the signal, the FFT will give 2 peaks (one at the actual frequency and one at sampling frequency minus actual frequency), making the second half of the magnitude vector a mirror image of the first half.

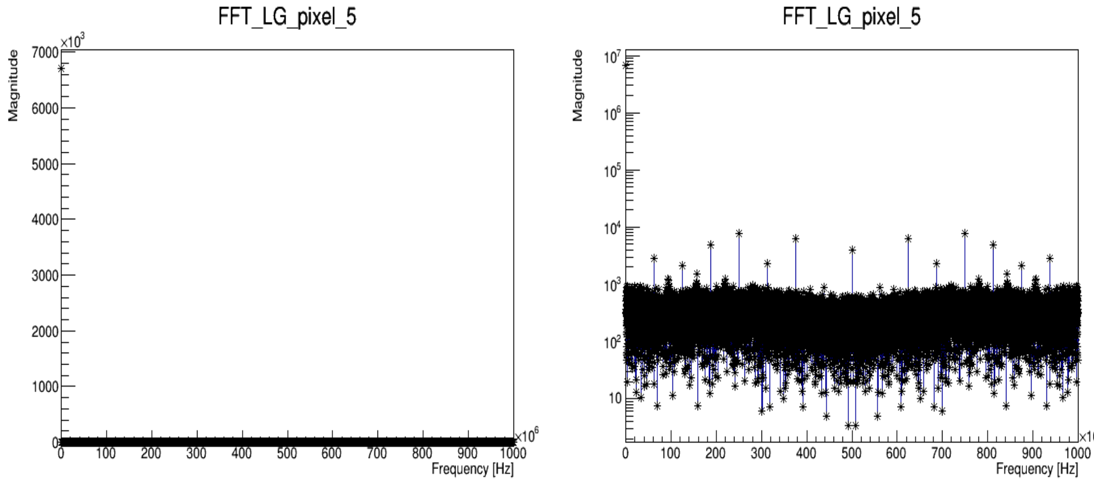

Figure 6.13. The Fourier transform of pixel 5 in the LG branch of board 1. On the right is the same plot plotted in logarithmic scale.

As seen in Fig. 6.13 and Fig. 6.14 there are also minor peaks in the spectrum in Fig. 6.11 and Fig. 6.12, which have even a bit larger magnitudes in the HG branch of the noisy part of the readout boards. There is a slight peak at around 420 MHz that appears to be in the high gain branch *only* and not in the low gain branch of the same channel. In some channels, there are minor peaks that seem to be at certain frequencies, for example at about 60, 150, 250, 350 MHz, (see appendix F for the full list).

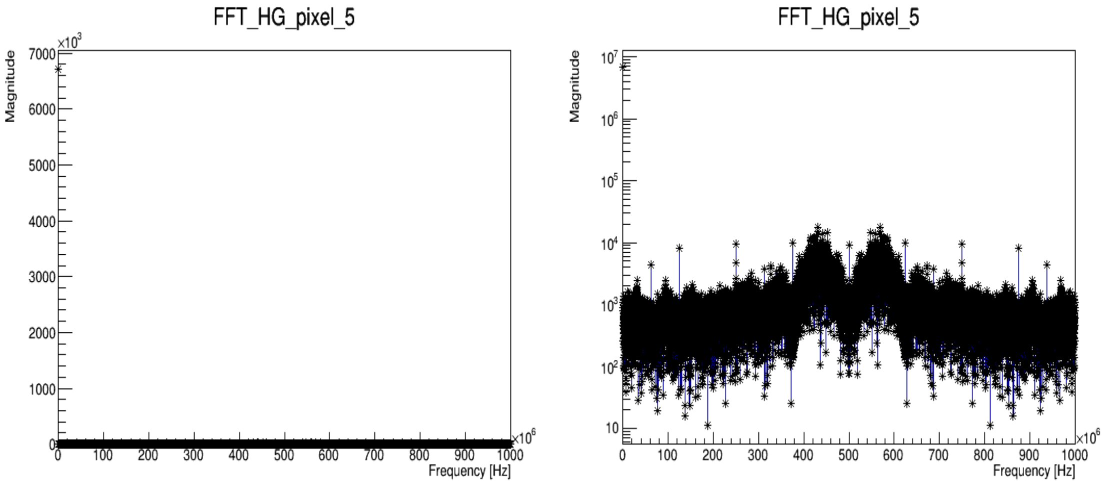

Figure 6.14. The Fourier transform of pixel 5 in the HG branch of board 1. On the right is the same plot plotted in logarithmic scale.

At the moment, reason for the observed peaks in the FFT is unknown. This is of course an interesting for further studies.

Chapter 7

Conclusion and outlook

A significant level of cross-talk in channel 5–8 of the analog boards of the upgraded H.E.S.S-I cameras has been observed. The study of electronic pedestals of these analog boards could help understand such observed level of cross-talk.

So far, from the computation of the autocorrelation function and the Fourier transforms of the electronic pedestals, no characteristic patterns (systematic repetition or periodicity) have been found to explain the level of cross-talk observed in channel 5–8 and 13–16 of the readout boards of the drawer.

It could also be due to the fact that the signals in channel 5-8 always have a *longer way* to travel than the signals in channels 1-4 (see Fig. 3.4), a bit more voltages might have been induced in these channels (channel 5-8), which might be a result of the observed cross-talk.

As seen in the distribution of the RMSes, the distributions have a large width in the high gain branches of the drawer, which suggests more noise in the data from the high gain branches as compared to the data from the low gain branches of the drawer. There are also significant outliers in the RMS distribution in both low and high gain and in some channels, the RMS distribution is bimodal. The distribution of the mean of events follow a normal distribution in the low and high gain branches of the drawer.

It is recommended to investigate the peaks present in the FFT in more detail, to study the time dependence of the found features or to systematically study the amplitude of the baseline shifts in more detail.

The upgrade of the cameras is ongoing, and the study of the impact of such level of electronic noise on the performance of the telescope is planned. This electronic noise might possibly lead to inaccurate interpretation of the data, thus a simulation study for both noise and cross-talk are recommended in order to check their significant influences on data quality.

Bibliography

[1] HESS Collaboration 2016 High energy stereoscopic system URL `https://www.mpi-hd.mpg.de/hfm/HESS/pages/about/`

[2] Giavitto G *et al.* 2015 A major electronics upgrade for the H.E.S.S. Cherenkov telescopes 1-4 *ArXiv e-prints* (*Preprint* `1509.01232`)

[3] Giavitto G *et al.* 2016 Upgraded cameras for the HESS imaging atmospheric Cherenkov telescopes *Society of Photo-Optical Instrumentation Engineers (SPIE) Conference Series* (*procspie* vol 9908) p 99082H

[4] Mazin D, Tescaro D, Garczarczyk M, Giavitto G, Sitarek J and for the MAGIC Collaboration 2014 Upgrade of the MAGIC telescopes *ArXiv e-prints* (*Preprint* `1410.5073`)

[5] Kieda D 2011 Status of the VERITAS Upgrade *International Cosmic Ray Conference* vol 9 p 14 (*Preprint* `1110.4360`)

[6] Punch M *et al.* 2000 GigaHertz Analogue Memories in ground-based gamma-ray astronomy *American Institute of Physics Conference Series* (*American Institute of Physics Conference Series* vol 515) ed Dingus B L, Salamon M H and Kieda D B pp 373–377

[7] Grieder P K F 2001 *Cosmic Rays at Earth* (Amsterdam, The Netherlands: Elsevier Science Gulf Professional Publishing)

[8] Todero Peixoto C J, de Souza V and Biermann P L 2015 Cosmic rays: the spectrum and chemical composition from 10^{10} to 10^{20} eV *Journal of Cosmology and Astroparticle Physics* vol 7 p 042 (*Preprint* 1502.00305)

[9] Degrange B and Fontaine G 2015 Introduction to high-energy gamma-ray astronomy *Comptes Rendus Physique* vol 16 pp 587–599 (*Preprint* 1604.05488)

[10] Schneider P 2006 *Extragalactic Astronomy and Cosmology*

[11] Abbasi R U *et al.* 2008 First Observation of the Greisen-Zatsepin-Kuzmin Suppression *Physical Review Letters* vol 100 p 101101 (*Preprint* astro-ph/0703099)

[12] Takeda M *et al.* 1998 Extension of the Cosmic-Ray Energy Spectrum beyond the Predicted Greisen-Zatsepin-Kuz'min Cutoff *Physical Review Letters* vol 81 pp 1163–1166 (*Preprint* astro-ph/9807193)

[13] Perkins D H 2003 *Particle astrophysics*

[14] Cui W 2009 TeV gamma-ray astronomy *Research in Astronomy and Astrophysics* vol 9 pp 841–860 (*Preprint* 0907.4052)

[15] Garmire G and Kraushaar W L 1965 High Energy Cosmic Gamma Rays *Springer* vol 4 pp 123–146

[16] Völk H J and Bernlöhr K 2009 Imaging very high energy gamma-ray telescopes *Experimental Astronomy* vol 25 pp 173–191 (*Preprint* 0812.4198)

[17] Protheroe R J and Kazanas D 1983 On the origin of relativistic particles and gamma-rays in quasars *Astrophysical Journal* vol 265 pp 620–624

[18] Thompson D J 2008 Gamma ray astrophysics: the EGRET results *Reports on Progress in Physics* vol 71 p 116901 (*Preprint* 0811.0738)

[19] The Fermi-LAT Collaboration 2015 Fermi-LAT Observations of High-Energy Gamma-Ray Emission Toward the Galactic Center *ArXiv e-prints* (*Preprint* `1511.02938`)

[20] 2009 The Principles of Astronomical Telescope Design *Astrophysics and Space Science Library* (*Astrophysics and Space Science Library* vol 360) ed Cheng J

[21] Matthews J 2005 A Heitler model of extensive air showers *Astroparticle Physics* vol 22 pp 387–397

[22] Chadwick P 2005 HESS High-energy astrophysics: Mapping the gamma-ray sky *Astronomy and Geophysics* vol 46 pp 6.12–6.15

[23] Watson A A 2011 The discovery of Cherenkov radiation and its use in the detection of extensive air showers *Nuclear Physics B Proceedings Supplements* vol 212 pp 13–19 (*Preprint* `1101.4535`)

[24] Balzer A 2010 *Systematic studies of the H.E.S.S. camera calibration* PhD dissertation Friedrich-Alexander-Universität Queensland University of Technology

[25] Schönwald A 2008 *Measurement of the cosmic ray flux with H.E.S.S* PhD dissertation Humboldt-Universität zu Berlin

[26] Buskirk F R and Neighbours J R 1986 Cerenkov radiation and electromagnetic pulse produced by electron beams traversing a finite path in air *NASA STI/Recon Technical Report N* vol 86

[27] Fülöp L and Biró T 1992 Cherenkov radiation spectrum *International Journal of Theoretical Physics* vol 31 pp 61–74

[28] de Naurois M and Mazin D 2015 Ground-based detectors in very-high-energy gamma-ray astronomy *Comptes Rendus Physique* vol 16 pp 610–627 (*Preprint* 1511.00463)

[29] Aleksić J *et al.* 2016 The major upgrade of the MAGIC telescopes, Part I: The hardware improvements and the commissioning of the system *Astroparticle Physics* vol 72 pp 61–75 (*Preprint* 1409.6073)

[30] de Naurois M and Rolland L 2009 A high performance likelihood reconstruction of γ-rays for imaging atmospheric Cherenkov telescopes *Astroparticle Physics* vol 32 pp 231–252 (*Preprint* 0907.2610)

[31] de Naurois M 2006 Analysis methods for Atmospheric Cerenkov Telescopes *ArXiv Astrophysics e-prints* (*Preprint* astro-ph/0607247)

[32] Holder J 2015 Atmospheric Cherenkov Gamma-ray Telescopes *ArXiv e-prints* (*Preprint* 1510.05675)

[33] Hinton J A and the HESS Collaboration 2004 The status of the HESS project *Nucleic Acids Research* vol 48 pp 331–337 (*Preprint* astro-ph/0403052)

[34] Bolmont J *et al.* 2014 The camera of the fifth H.E.S.S. telescope. Part I: System description *Nuclear Instruments and Methods in Physics Research A* vol 761 pp 46–57 (*Preprint* 1310.5877)

[35] Funk S Funk S 2015 Space- and Ground-Based Gamma-Ray Astrophysics *ArXiv e-prints* (*Preprint* 1508.05190)

[36] Benbow W 2006 The H.E.S.S. Experiment *Particles and Nuclei* (*American Institute of Physics Conference Series* vol 842) ed Barnes P D, Cooper M D, Eisenstein R A, van Hecke H and Stephenson G J pp 998–1000

[37] Bernlöhr K *et al.* 2003 The optical system of the H.E.S.S. imaging atmospheric Cherenkov telescopes. Part I: layout and components of the system *Astroparticle Physics* vol 20 pp 111–128 (*Preprint* `astro-ph/0308246`)

[38] Krayzel *et al* Krayzel *et al* 2013 Improved sensitivity of H.E.S.S.-II through the fifth telescope focus system *ArXiv e-prints* (*Preprint* `1307.6461`)

[39] Tluczykont M, Hampf D, Horns D, Spitschan D, Kuzmichev L, Prosin V, Spiering C and Wischnewski R 2014 The HiSCORE concept for gamma-ray and cosmic-ray astrophysics beyond 10 TeV *Astroparticle Physics* vol 56 pp 42–53 (*Preprint* `1403.5688`)

[40] Hörandel J R 2013 The composition of cosmic rays at the knee *American Institute of Physics Conference Series* (*American Institute of Physics Conference Series* vol 1516) ed Ormes J F pp 185–194 (*Preprint* `1212.0739`)

[41] Acero F *et al.* 2010 First detection of VHE γ-rays from SN 1006 by HESS *ArXiv e-prints* vol 516 p A62 (*Preprint* `1004.2124`)

[42] Hofmann W and HESS Collaboration 2000 The high energy stereoscopic system (HESS) project *American Institute of Physics Conference Series* (*American Institute of Physics Conference Series* vol 515) ed Dingus B L, Salamon M H and Kieda D B pp 500–509

[43] Balzer A, Füßling M, Gajdus M, Göring D, Lopatin A, de Naurois M, Schlenker S, Schwanke U and Stegmann C 2014 The H.E.S.S. central data acquisition system *Astroparticle Physics* vol 54 pp 67–80 (*Preprint* `1311.3486`)

[44] Bradascio F 2014 Characterisation of the readout for the H.E.S.S.-I Upgrade pp 1–14

[45] Aharonian F *et al.* 2004 Calibration of cameras of the H.E.S.S. detector *Astroparticle Physics* vol 22 pp 109–125

[46] Funk S 2005 *A new population of very high-energy γ-ray sources detected with H.E.S.S. in the inner part of the Milky Way* PhD dissertation MPI for Nuclear Physics

[47] Apicella B, Bruno A, Wang X and Spinelli N 2013 Fast Fourier Transform and autocorrelation function for the analysis of complex mass spectra *International Journal of Mass Spectrometry* vol 338 pp 30–38

[48] Brockwell P J and Davis R A 2001 *Introduction to Time Series and Forecasting* (Springer International Publishing)

[49] Press W H, Teukolsky S A, Vetterling W T and Flannery B P 2007 *Numerical recipes in C++ : the art of scientific computing* vol 31 (Cambridge University Press)

Appendix A

Electronic pedestal waveforms

Electronic pedestal waveforms for a single event for board 1 of the drawer.

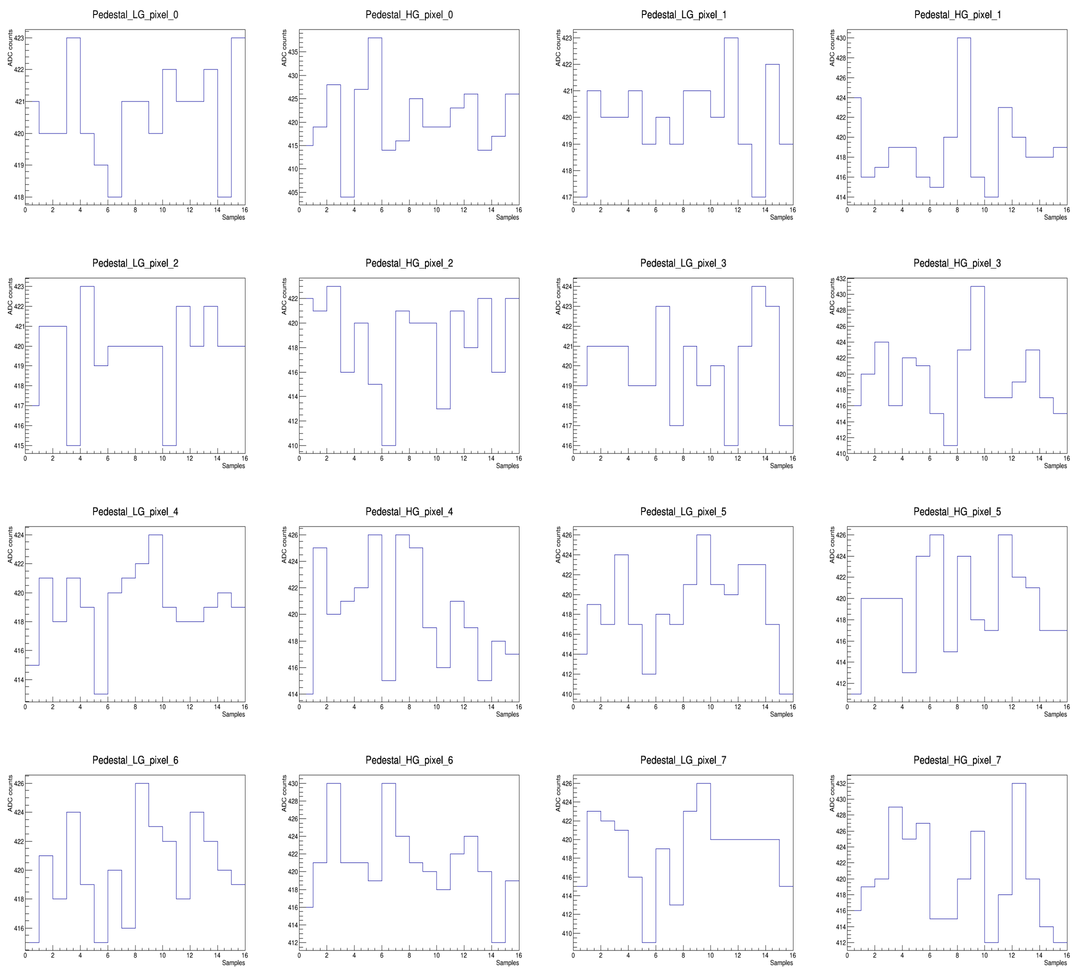

Electronic pedestal waveforms for a single event for board 2 of the drawer.

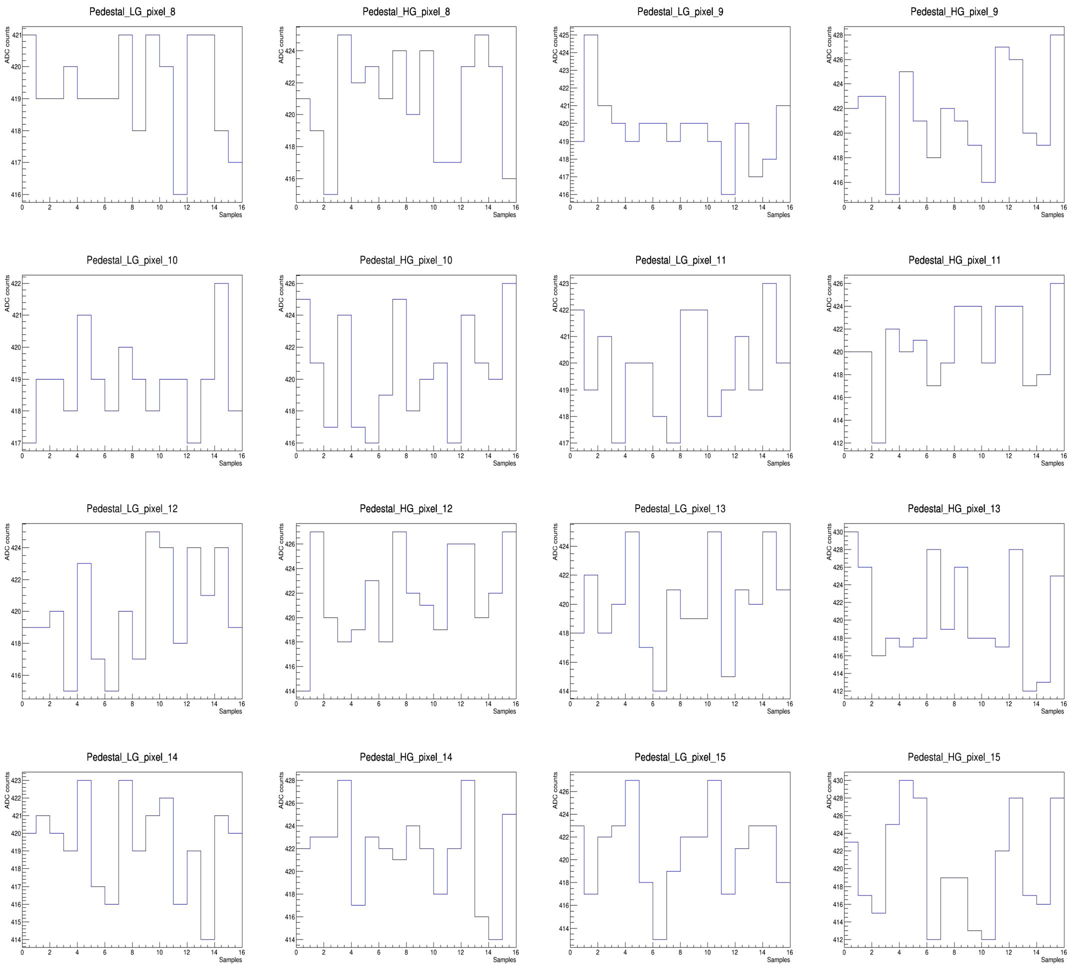

Appendix B

Autocorrelation

Autocorrelation for the LG and HG branches of board 1 of the drawer.

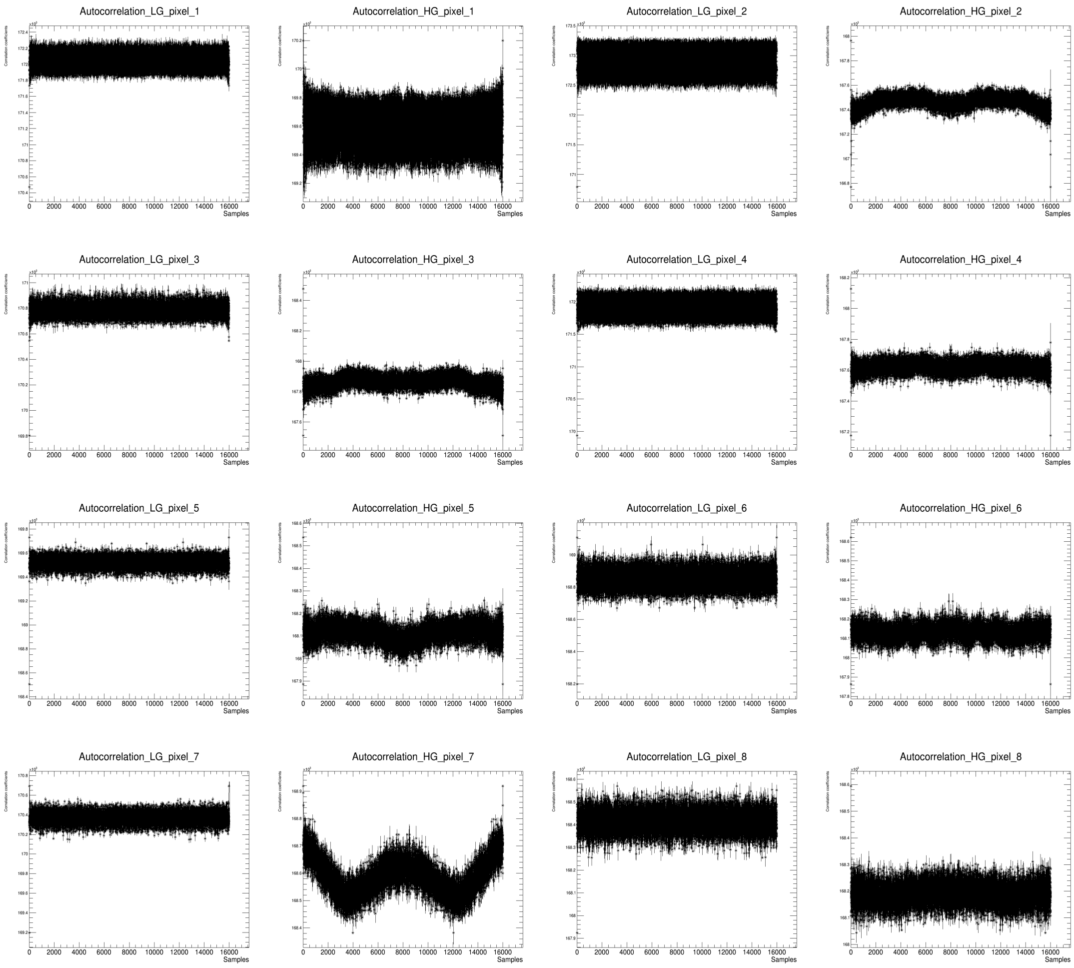

Autocorrelation for the LG and HG branches of board 2 of the drawer.

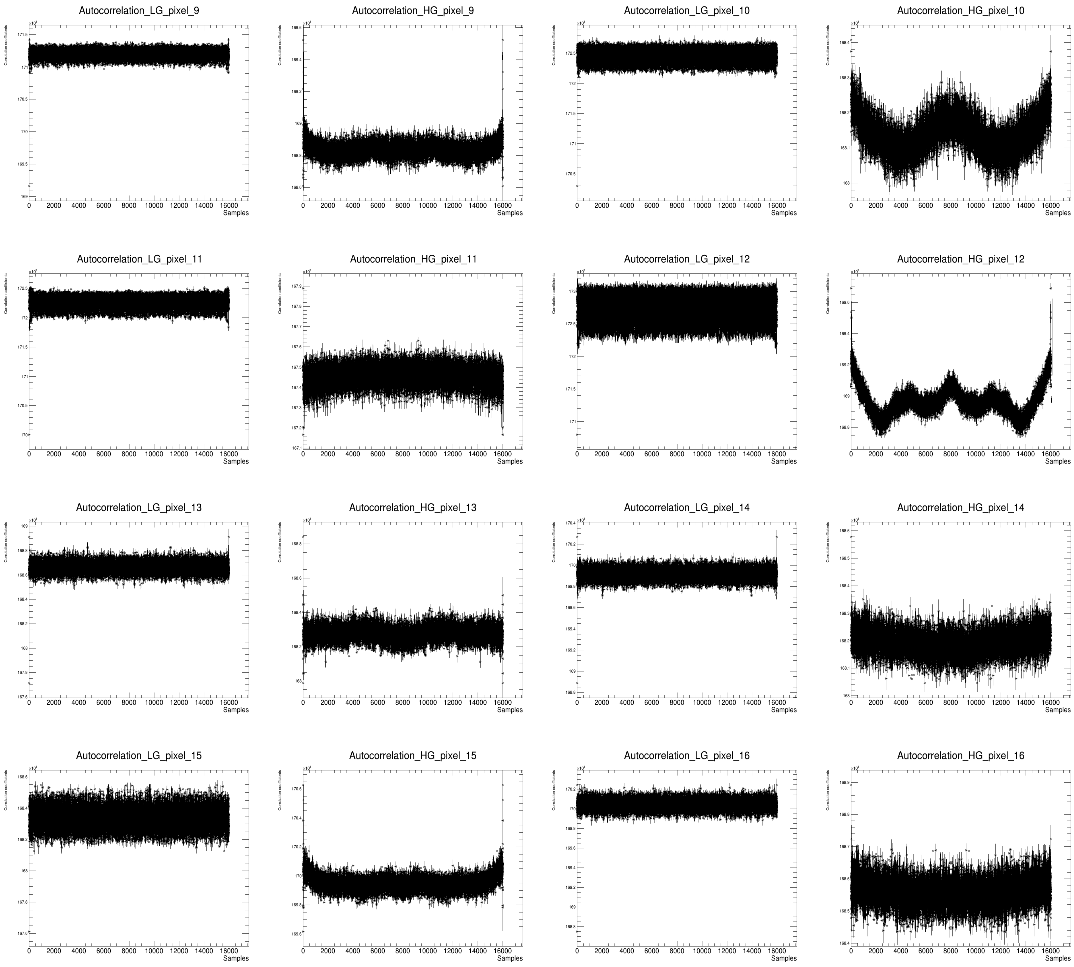

Appendix C

Pixel to pixel correlation

Pixel to pixel correlation for board 1 in LG and HG branches of the drawer.

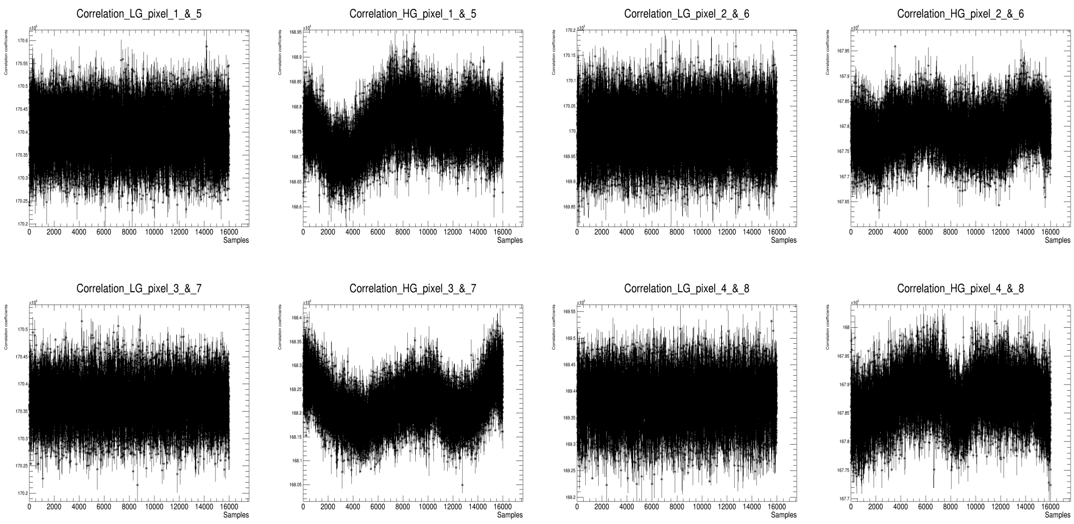

Pixel to pixel correlation for board 2 in LG and HG branches of the drawer.

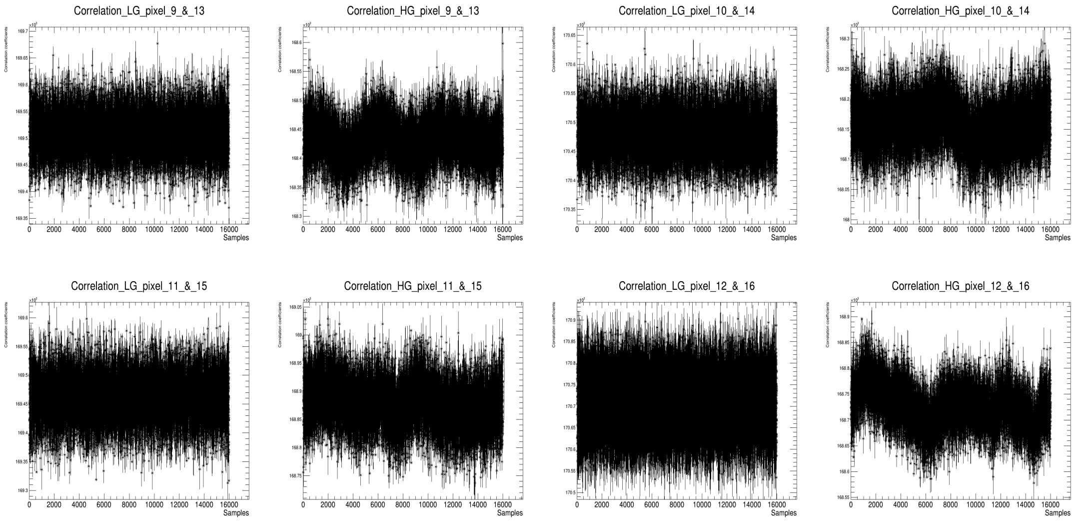

Appendix D

Distribution of the Mean

The distribuion of the Mean in the LG and HG branches of board 1 of the drawer.

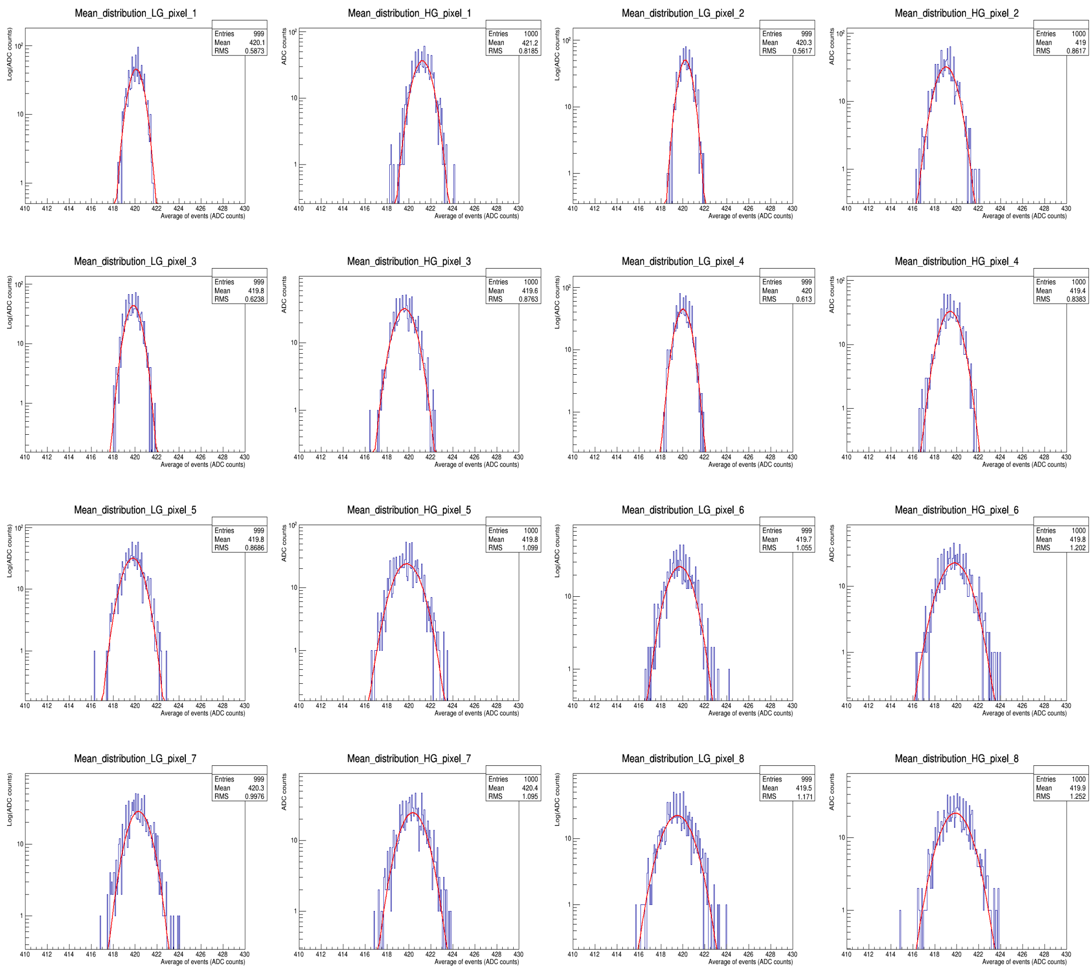

The distribuion of the Mean in the LG and HG branches of board 2 of the drawer.

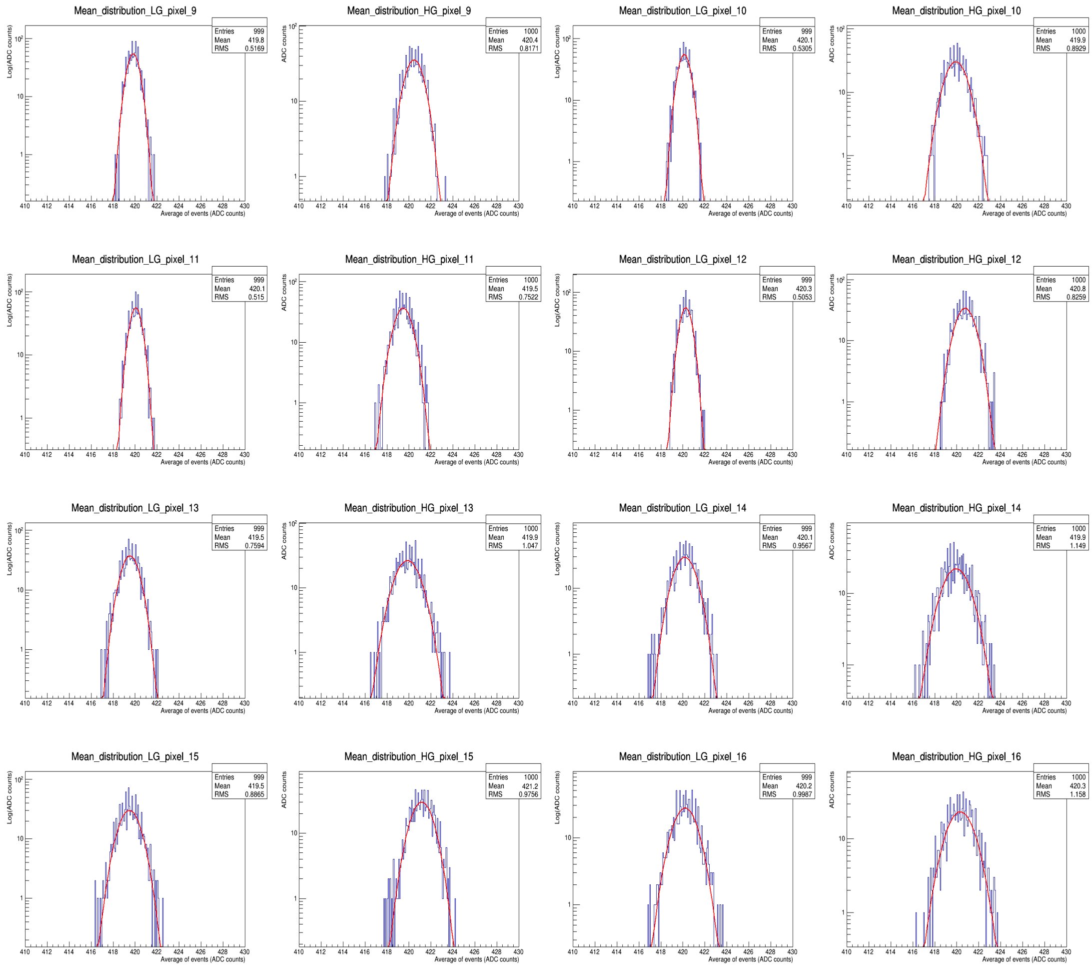

Appendix E

RMS distribution

The distribuion of the RMS in the LG and HG branches of board 1 of the drawer.

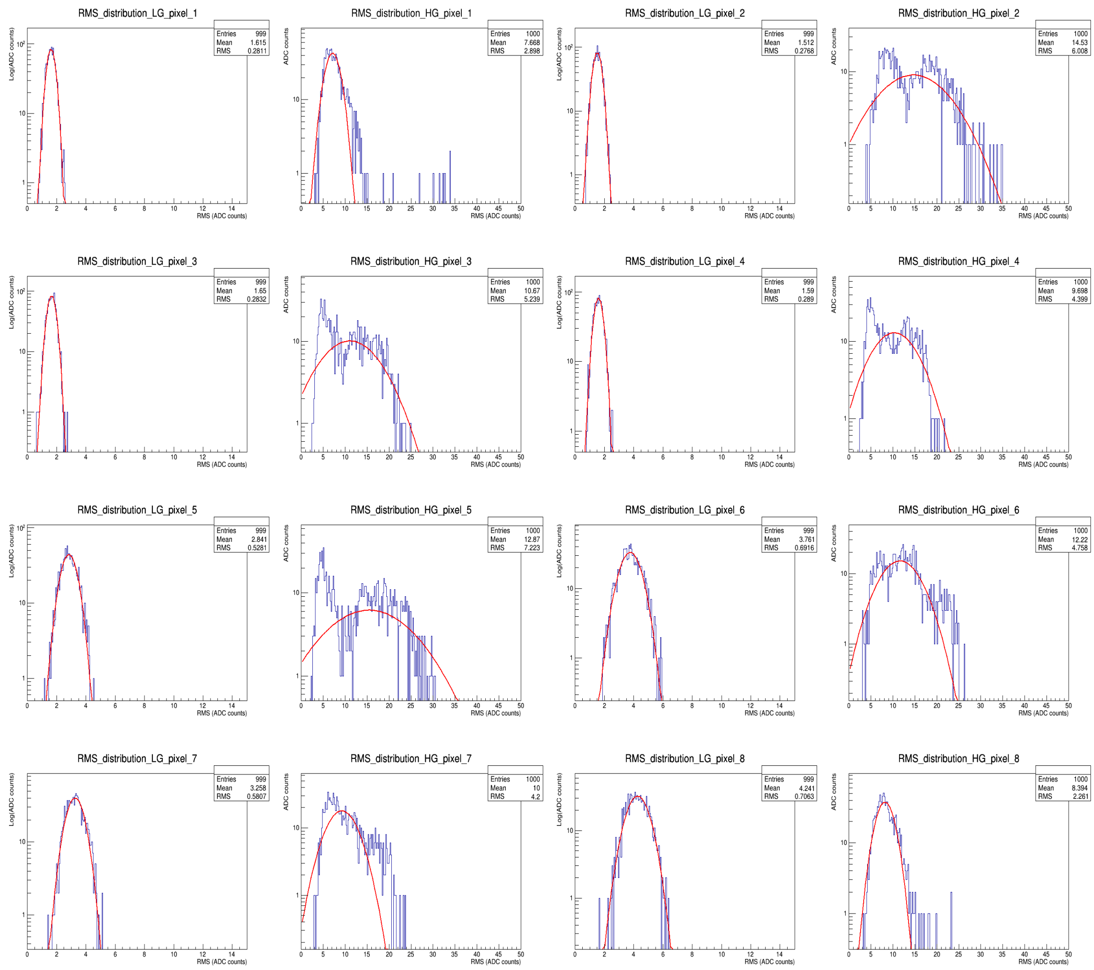

The distribuion of the RMS in the LG and HG branches of board 2 of the drawer.

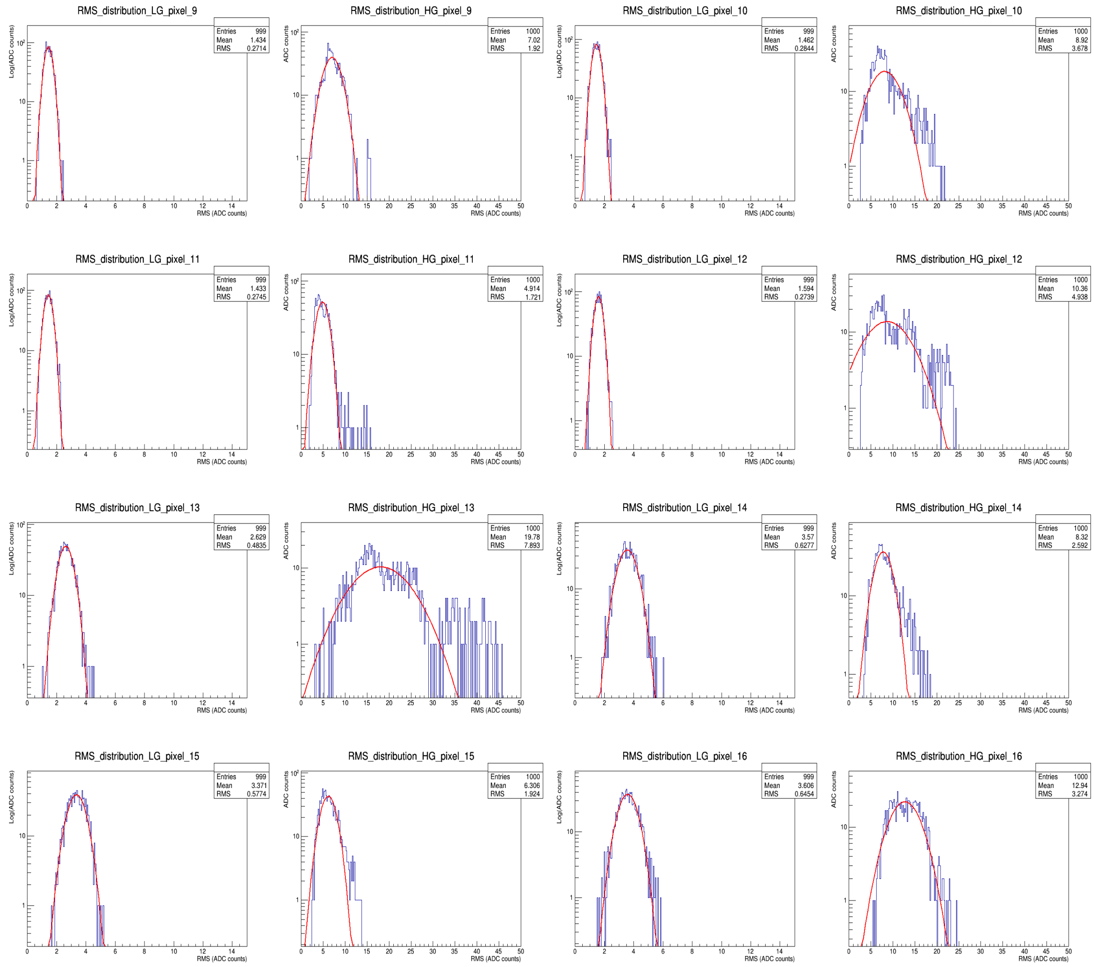

Appendix F

Fourier transform

Fourier transform of all channels in the **LG** branch of **board 1** of the drawer.

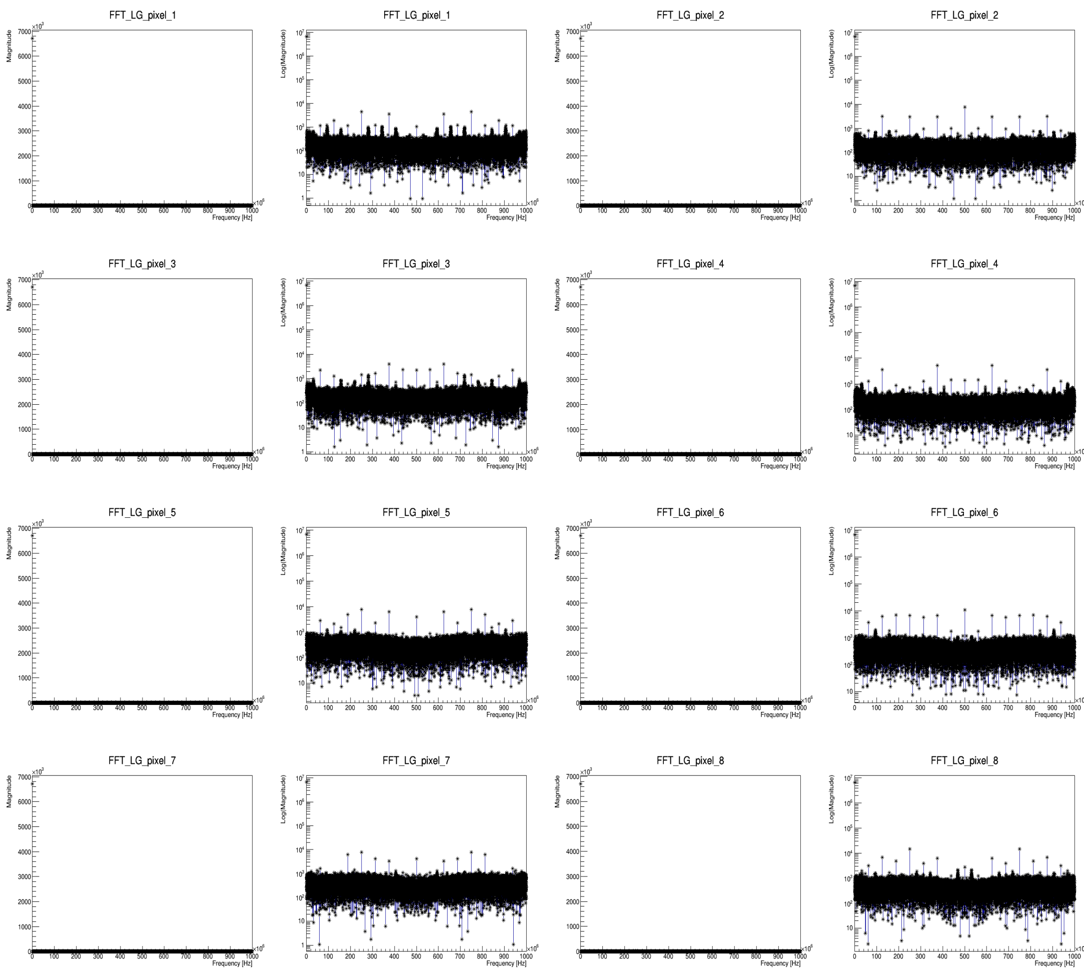

Fourier transform of all channels in the **HG** branch of **board 1** of the drawer.

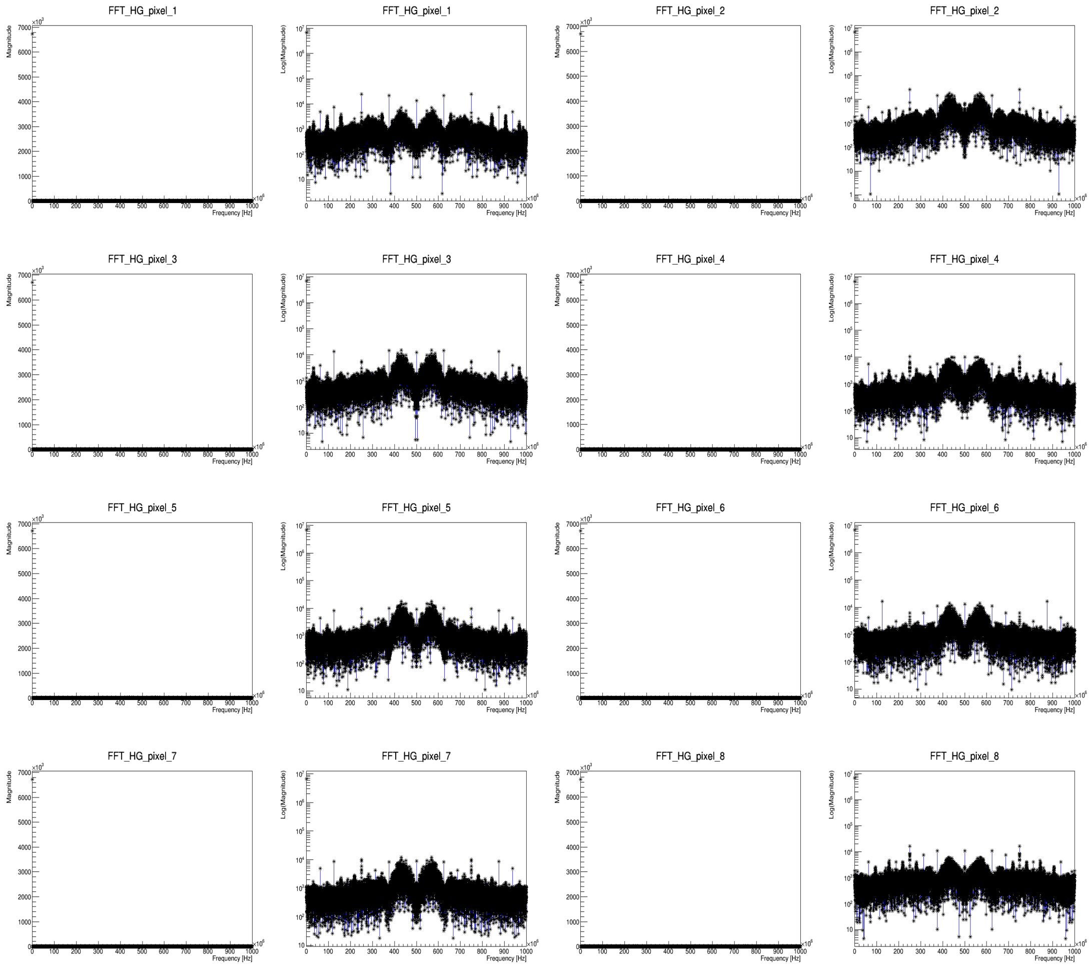

Fourier transform of all channels in the **LG** branch of **board 2** of the drawer.

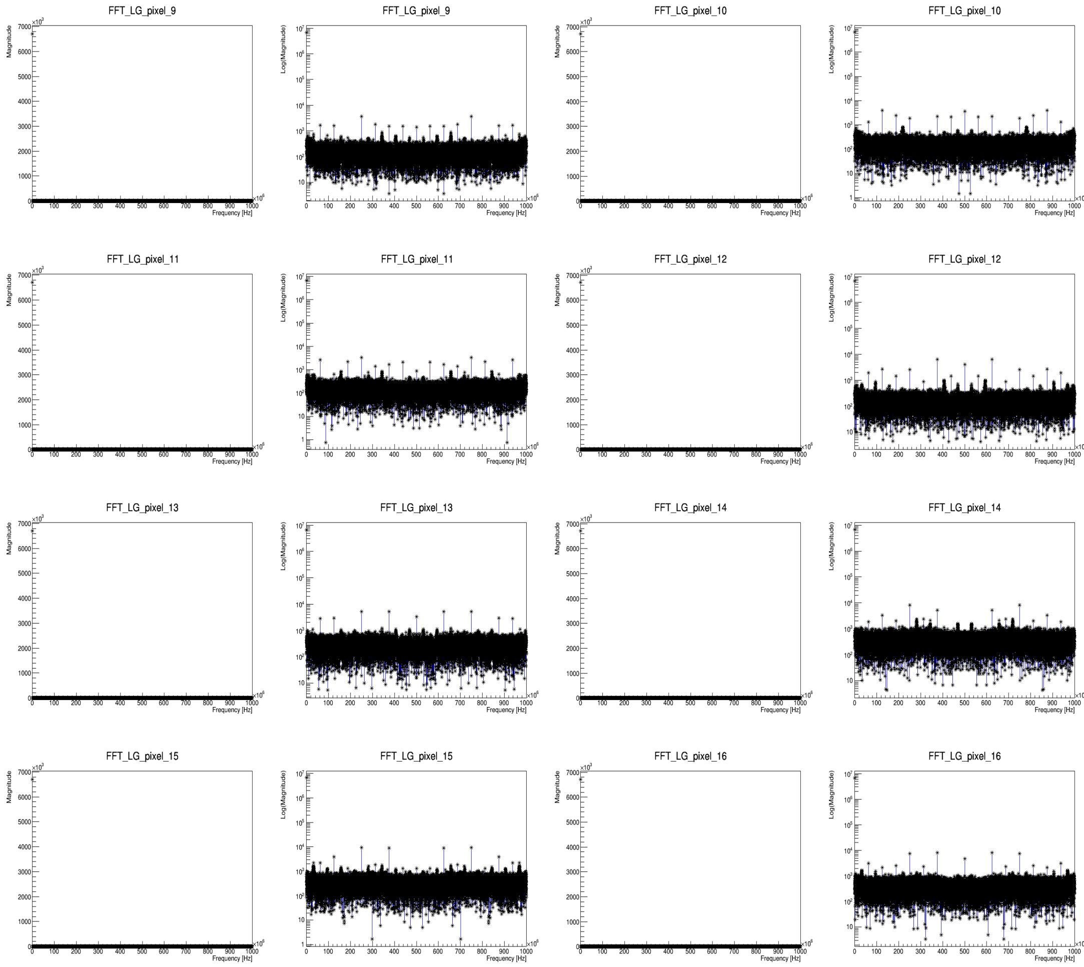

Fourier transform of all channels in the **HG** branch of **board 2** of the drawer.